

POLITECNICO DI MILANO

Scuola di Ingegneria Industriale e dell'Informazione

Corso di Laurea Magistrale in Ingegneria Biomedica



Sensors for Curvature Estimation in Electrical Impedance Tomography Belt

Relatore: Prof. Pietro Cerveri

Correlatore: Prof. Chi-Nan Pai

Giulia Avallone Mendonça

10529790

Anno accademico 2016/2017

POLITECNICO DI MILANO

Sensors for Curvature Estimation in Electrical Impedance Tomography Belt

Final thesis presented at Politecnico di Milano - Scuola di Ingegneria Industriale e dell'Informazione as requirement to obtain the degree of Master of Science in Biomedical Engineering - Electronic Technologies

Giulia Avallone Mendonça

Relatore: Prof. Pietro Cerveri

Correlatore: Prof. Chi-Nan Pai

Milano

Anno accademico 2016/2017

To my parents and sister

ACKNOWLEDGEMENTS

This thesis might not have been possible without the help of Prof. Pietro Cerveri and Prof. Chi-Nan Pai, who supported me since the beginning and taught me that knowledge goes beyond the limits of the classrooms and laboratories. The experience and time they give to me could not be more gratifying.

In every day's rush we might forget to say thanks to the people around us, for that reason I would like to express my gratitude, especially, to my parents and sister, who have always been with me in the sad and happy moments during my studies.

Of course, all this encouragement was not offered just from my family. I have been accompanied by special people, both in Brazil and in Italy, who have made this journey easier and unforgettable. I will always keep them in my heart.

Finally, I would like to thank Politecnico di Milano, Escola Politécnica of São Paulo and CAPES - Coordenação de Aperfeiçoamento de Pessoal de Nível Superior for educational and financially helping me to achieve my dream.

ABSTRACT

The Electrical Impedance Tomography (EIT) is a relevant imaging method especially for patients submitted to mechanical ventilation which require constant monitoring. This type of tomography is interesting for its low-cost compared to other types of tomography, its easy applicability in Intensive Care Units (ICU) and its absence of adverse effects in clinical applications even over long-time exposure.

However, the images produced by EIT still presents a significant quantity of artifacts and other accuracy errors due to the inexactness of estimations of electrode's position and reconstruction domain's shape. The solutions until then were not enough to solve these issues.

This work purposes to create an electronic system, additional to existing electrodes belt, able to reconstruct the body shape contour and to identify the positions of electrodes around it.

Based on strain gauge technology, an electronic circuit is developed to sense the deflection of the belt. This information is the starting point for a mathematical method that models mechanical behavior of the belt, aiming to reconstruct the corporeal curvature.

Simulations and empirical tests are done to prove the concept of this work and to quantify the applicability of the system to actual clinical results of EIT.

Key-words: Electrical Impedance Tomography, Mechanical Ventilation, Biomedical Instrumentation.

SOMMARIO

La tomografia ad impedenza elettrica (EIT) è un rilevante metodo per la creazione di immagini, specialmente per pazienti sottoposti a ventilazione meccanica perché richiede un monitoraggio costante. Questo tipo di tomografia è interessante rispetto alle altre tecnologie per il suo basso costo, per la sua facilità di applicazione nei centri di cura intensiva (ICU) e per l'assenza di effetti negativi dovuti a una lunga esposizione.

Tuttavia, le immagini prodotte dall'EIT ancora presentano una significativa quantità di imprecisioni ed errori dovuti all'inesattezza della stima della posizione degli elettrodi e della ricostruzione della curva. Le soluzioni proposte fino a ora non sono state capaci di risolvere questi problemi.

Lo scopo di questo lavoro è di creare un sistema elettronico, collegato a una cintura di elettrodi, capace di ricostruire il contorno della curva toracica umana e identificare la posizione degli elettrodi attorno a essa.

Basandosi sulla tecnologia degli strain gauges, è stato sviluppato un circuito elettrico per rilevare la curvatura della cintura. Questa informazione è l'input di un modello matematico che analizza il comportamento meccanico della cintura, con lo scopo di ricostruire la curvatura corporea.

Simulazioni e prove empiriche sono state effettuate per verificare questo lavoro e valutare l'applicabilità ad attuali usi clinici dell'EIT.

Parole chiave: Tomografia ad Impedenza Elettrica, Ventilazione Meccanica, Strumentazione Biomedica

CONTENTS

1	INTRODUCTION	1
1.1	Electrical Impedance Tomography	1
1.2	Motivation and objectives	3
1.3	Expected results	5
2	STATE-OF-THE-ART	6
2.1	Simultaneous reconstruction method	6
2.2	Compensation of modelling errors	9
2.3	Computer vision	11
2.3.1	Optical Localizers	12
2.3.2	3D scanning	15
2.4	Optical fiber	17
2.5	Strain gauge	17
3	MATERIALS AND METHODS	20
3.1	Shape identification device	20
3.1.1	Belt configuration	20
3.1.2	Strain gauge	22
3.1.3	Electronic circuit	26
3.1.4	Calibration procedure	30
3.2	Curvature reconstruction method	31
3.2.1	Curvature of the part of belt with strain gauges	32
3.2.1.1	Linear approximation	34
3.2.1.2	Circumference approximation	35
3.2.2	Curvature of the part of belt between strain gauges	37
3.2.2.1	Curvature interpolation model	37
3.2.2.2	Curvature integration	38
3.3	Curvature simulation	41
3.3.1	Error propagation	43
3.4	System evaluation methods	44
3.4.1	Precision	45

3.4.2	Accuracy	46
4	RESULTS	47
4.1	Shape identification device	47
4.1.1	Belt configuration	47
4.1.2	Electronic circuit	48
4.1.3	Calibration results	49
4.2	Curvature simulation	50
4.2.1	Distance between two strain gauges	50
4.2.2	Body radius variation	52
4.2.3	Elliptical body shape	53
4.3	System evaluation	55
5	DISCUSSION AND CONCLUSION	59
	BIBLIOGRAPHY	61

LIST OF FIGURES

Figure 1.1 – Block diagram of EIT system for thorax imaging extracted from Adler et al. (1997)	3
Figure 2.1 – One of experimental evaluation results extracted from Dardé et al. (2013a) . First column: photos of the targets (top: two plastic cuboids; middle: a hollow steel cylinder; bottom: a hollowsteel cylinder and a plastic cuboid). Second column: reconstructions with an incorrect geometry. Third column: reconstructions with an (almost) accurate geometry. Fourth column: simultaneous reconstructions of the geometry and the conductivity by the full algorithm.	8
Figure 2.2 – 3-D example of compensation error modeling method with experimental data from a thorax shaped measurement tank taken from (NISSINEN et al., 2011). The measurement phantom and MAP estimates with real data. The images show the central horizontal cross sections from the 3-D reconstructions. N_n is the number of nodes in the forward mesh.	10
Figure 2.3 – Application of optical markers in (a) entertainment and (b) sports medicine.	13
Figure 2.4 – Optical measurement systems from ©2017 Northern Digital Inc..Images taken from (Northern Digital Inc., 2017)	14

Figure 2.5 – Extracted from (NEWCOMBE et al., 2011). Results from circular motion experiences. For each column, the top row shows the estimated sensor trajectory and the bottom row reconstruction view. (a) Frame-to-frame tracking, where the pose of each new frame is estimated by registration against just the last frame. Poor reconstruction due to non-circular trajectory. (b) Processing is halted with the loop two-thirds complete. (c) shows loop closure, where the last frame processed is a duplication of the first frame. (d) same data from (c) and taken repeatedly.	16
Figure 2.6 – Several bounded and unbounded metal and semiconductor strain gauges (from BHL electronics)	18
Figure 3.1 – (a) and (b) belong to EIT system PulmoVista 500 from Drägerwerk AG & Co. KGaA. The belt contains 16 electrodes placed around the chest wall with circumference varying from 70 cm to 150 cm. Taken from (TESCHNER et al., 2010).	21
Figure 3.2 – Device model: (a) highlights system’s application inside existing EIT belts while (b) illustrates sensing belt architecture.	22
Figure 3.3 – When bar strain is the effect of an uniaxial force, there is a change of length l of material proportional to cross sectional area, A , and to an applied force, F	22
Figure 3.4 – Bonded Metallic Strain Gauge - most widely used gauge. Extracted from National Instruments (1998)	25
Figure 3.5 – Full Wheatstone bridge	27
Figure 3.6 – Best bridge configuration for bending strain	27
Figure 3.7 – Bridge amplifier scheme taken from Burr-Brown Corporation (1996)	28
Figure 3.8 – Basic connections of INA129PA circuitry from Burr-Brown Corporation (1996)	29
Figure 3.9 – Full conditioning circuit	30

Figure 3.10–Representation of flat calibrated position for a sensing belt segment. The light gray rectangle represents the sensing segment which is centered on its own frame n .	33
Figure 3.11–Signal definition to represent curvature orientation according to sensing circuit arrangement	33
Figure 3.12–Estimation of bending displacement of a sensing segment as straight lines profile.	34
Figure 3.13–Estimation of bending displacement of a sensing segment as circumference arc profile.	35
Figure 3.14–Positive and negative auxiliary frames are attached to the extremities of the estimated curve. i axis has same direction of tangent in that point. It is done similarly to interpolation curves.	39
Figure 3.15–Schematic of homogeneous transformation between the curve estimation n and the interpolating curve m using auxiliary frames to guarantee continuity.	40
Figure 3.16–Simulated body shape has circular profile, represented centered in the reference system with axes x and y . Straight element layed on upper-most point of the circumference is a segment of tangent line in that point with dimension equal to strain gauge nominal length. . .	41
Figure 3.17–Simulated body shape has ellipsoidal profile, represented centered in the reference system with axes x and y . Strain is considered as the length difference between tangent segment on that point with strain gauge nominal dimension and a circumference arc with radius equal to the distance of the point and ellipse center. Each point of the ellipsoid has equivalent strain approximation of a circumference of radius equal to the distance between ellipse center and the point itself.	42
Figure 3.18–Specimens used in experimentation to simulate range of human body thorax dimensions.	44

Figure 4.1 – Yellow backing material over which strain gauges are fixed with glue and their cables set stable with black insulating tape. The total test belt is composed by 3 sensing segments and two sensing gaps equally distributed.	47
Figure 4.2 – (a) and (b) are taken from (HOFFMANN, 1989). Dashed line represents the third cycle of rising and falling strain loads while the whole line is resultant of the first cycle. Z 70 is a cold curing rapid adhesive based on cyano acrylate, X 60 is also a cold curing rapid adhesive but based on polymethacrylate and the two adhesives EP 250 and EPY 550 are hot curing epoxy resin adhesives	51
Figure 4.3 – Simulation results for distance between two strain gauges. The distances selected are proportional to the nominal length of strain gage sensor and the body radius is constant 100 mm. (a) refers to a distance equal to the nominal length. (b) is the result for a distances between two strain gages equal to three times the nominal length of the sensors.	52
Figure 4.4 – Simulation results body radius variation within the range of human thorax dimensions.(a) is the simulation for a circular body shape with radius of 200 mm. (b) is the result for a circular body shape with radius of 50 mm .	53
Figure 4.5 – Testing proportion between semi-major, a and semi-minor axes, b , of elliptical profile. Simulation results body format variation within the ranges of human thorax. On left side, linear approximation is represented (blue). On right side, mid-curve estimation is represented (blue). Red line is the expected curve.	54
Figure 4.6 – Experience with belt in neutral flat position. Data Log of Arduino board is the upper-most plot, in which is possible to notice that three sensors have strain in zero position. Second graph is resultant of reconstruction method applied in neutral position: magenta line is the reconstructed final curve.	55

Figure 4.7 – Mean curve for specimen of $D = 50mm$ obtained after reconstruction method is represented by magenta line, while the yellow one is the expected curve of the body. 56

Figure 4.8 – Mean curve for specimen of $D = 200mm$ obtained after reconstruction method is represented by magenta line, while the yellow one is the expected curve of the body. 58

LIST OF TABLES

Table 1.1 – Conductivity values of different biological tissues <i>in vitro</i> at 125 kHz from Gabriel et al. (1996)	1
Table 3.1 – Data-sheet relevant information for strain gauge model PA-06-250BA-120 provided by Excel Sensores IND. COM. EXPORT.LTDA	25
Table 3.2 – Temperature self-compensation behavior for strain gauge model PA-06-250BA-120 provided by Excel Sensores IND. COM. EXPORT. LTDA	26
Table 4.1 – Elements selection according to circuitry project.	49
Table 4.2 – Error index values for tests in specimen with $D = 50mm$	57
Table 4.3 – Error index values for tests in specimen with $D = 200mm$	58

LIST OF ABBREVIATIONS AND ACRONYMS

EIT	<i>Electrical Impedance Tomography</i>
ICU	<i>Intensive Care Unit</i>
CT	<i>Computed Tomography</i>
MRI	<i>Magnetic Resonance Imaging</i>
FEM	<i>Finite Element Method</i>
CEM	<i>Complete Electrode Model</i>
OCR	<i>Optical Character Recognition</i>
MVS	<i>Multi-view Stereo</i>
SFM	<i>Structure from Motion</i>
NCSRR	<i>National Center for Simulation in Rehabilitation Research</i>
IR	<i>Infra-red</i>
MOCAP	<i>Motion Capture Systems</i>
CAS	<i>Computer Aided Surgery</i>
OCR	<i>Optical Character Recognition</i>
INA	<i>Instrumentation Amplifier</i>

1 INTRODUCTION

The intent of this thesis is to propose a system able to identify electrode positioning and body shape curvature in an Electrical Impedance Tomography (EIT) belt. In the following sections, the EIT scenario and this project motivations are detailed.

1.1 Electrical Impedance Tomography

Electrical Impedance Tomography is a non-invasive imaging technique based on the estimation of electrical impedance distribution inside a physical body from boundary electrical measurements. EIT has been applied in distinct study fields: medical imaging, nondestructive testing of materials, geophysics and environmental monitoring.

Particularly, EIT clinical use derives from the difference of electrical conductivity in biological tissues. Some tissues contain more ions, which act as charge carriers, than others, being able to better conduct electricity. This contrast between tissues, see table 1.1, makes it possible to image the impedance distribution.

Table 1.1 – Conductivity values of different biological tissues *in vitro* at 125 kHz from [Gabriel et al. \(1996\)](#)

Tissue	Conductivity (S m ⁻¹)
Skeletal muscle	3.671×10^{-1}
Fat	2.447×10^{-2}
Lung (inflated)	1.090×10^{-1}
Lung (deflated)	2.751×10^{-1}
Blood	7.044×10^{-1}
Blood vessel	3.193×10^{-1}
Liver	9.011×10^{-2}
Stomach	5.371×10^{-1}
Kidney	1.761×10^{-1}
Cortical bone	2.086×10^{-2}
Trabecular bone	8.409×10^{-2}

Applications in healthcare are numerous, EIT technique has been examined in non-invasive cardiac functions and blood flow monitoring, internal hemorrhage detection, breast cancer diagnosis, digestive system studies and brain function imaging (CHENEY et al., 1999; HOLDER, 2004).

However, utilization on respiratory medicine seems to be the most developed and promising one. According to Costa et al. (2009) current studies in this area are related to the care of critical patients such as the estimation of perfusion/ventilation during mechanical ventilation procedure, assessment of lung recruitment and lung collapse, detection of pneumothorax and pleural effusion and verification of correct placement of endotracheal tube. The current acceptance of EIT is due to the clinical advantages it might bring regarding other imaging methods:

- low cost, e.g., with respect to X-rays Computed Tomography (CT) and Magnetic Resonance Imaging (MRI) modalities
- there are not any known adverse effects from the clinical use of EIT even over long-time monitoring
- great time resolution that allows fast functional changes to be studied
- easy applicability in controlled environments as in Intensive Care Units (ICU)

Despite the variety of clinical uses EIT might allow, the reference scheme of this project is one for the thorax imaging, represented in figure 1.1. Typically, the system is composed by an array of 16 or 32 electrodes posed around the thorax. Low-amplitude and high-frequency current, commonly set to 5 mA and 50 kHz, is applied between a pair of electrodes and has different flowing pathways according to chest wall shape and thoracic distribution of impedivities. The resulting electric potentials on the surface are sampled by remaining electrodes. This process is then repeated for current injection into all electrodes to obtain the electrical impedance distribution using reconstruction algorithms.

Nevertheless, image reconstruction is the most demanding phase in EIT as it evolves the solution of a ill-posed non-linear problem. It means that

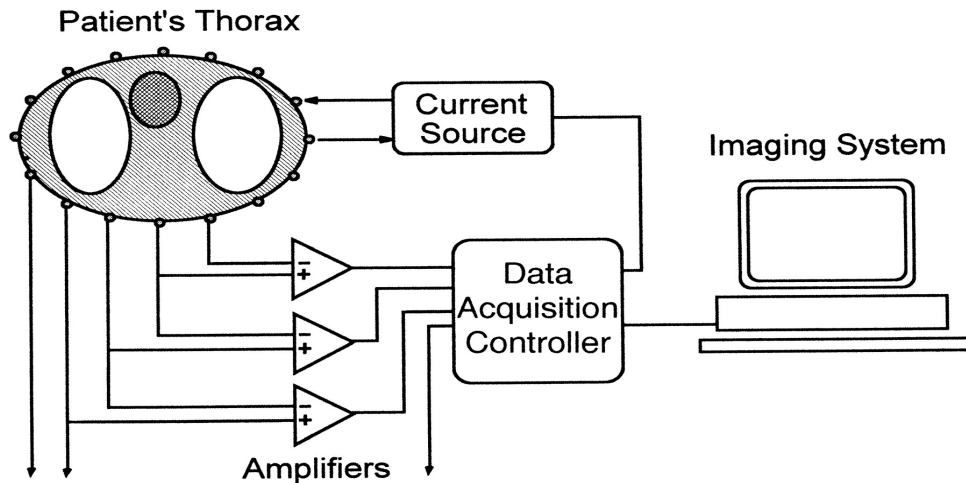


Figure 1.1 – Block diagram of EIT system for thorax imaging extracted from [Adler et al. \(1997\)](#)

small errors in voltage measurements may lead to fairly different solutions for impedance estimation. Moreover, the unfeasibility of increasing the number of electrodes, due to problems of attachment and maintenance of adequate signal to noise ratio, aggravates image reconstruction limiting the number of measurements at the body surface.

Different approaches were developed over the years to solve the reconstruction problem on EIT, e.g., Newton-Raphson, extended Kalman filter, Markov Chain Monte Carlo, back-projection over equipotential lines and sensibility method. A comparison between them can be found in the work done by [Yorkey e Webster \(1987\)](#).

1.2 Motivation and objectives

Contrarily to conventional medical imaging modalities, that uses high energy radiation beam to locally affect the matter along its path, in EIT, the application of electrical current is no longer a local effect. Due to non-locality, a system of simultaneous equations relating every voxel to every measurement must be solved to find conductivity image, relying on knowledge of electrode positions and potential differences for uniform conductivity.

Nevertheless, in real-life measurements there are more unknowns than the admittivity distribution since the exact electrode locations, the contact

impedance and the shape of the object are often not known accurately. The simplest solution to these obstacles is to set the electrodes into the wall of a cylindrical tank and make uniform measurements by filling the tank with saline, then inserting the object to be measured inside the tank (BARBER; BROWN, 1984).

In an *in vivo* measurement, however, there is no such possibility and the mismatch between the measured data and the prediction model is dominated mostly by the errors due to these three main unknown variables: electrode position, body shape and contact impedance (HOLDER, 2004).

Moreover, analyzing the influence of boundary shape, commonly modeled by a circle, on reconstructed image, Lionheart (1998) concludes that in the generic case, errors in shape cannot be exactly compensated for by a change in the conductivity.

Thus, the identification of electrode positioning and body shape during the EIT measurement acquisition might lead to the improvement of image quality, significantly reducing the occurrence of artifacts (SOLEIMANI et al., 2006; GÓMEZ-LABERGE; ADLER, 2008; JEHL et al., 2015).

Motivated by the enhancement of images caused by a proper body shape and electrode positioning identification in EIT, additionally to the significance of this imaging system in ICU patients under mechanical ventilation, the intent of this thesis is to develop a system able to overcome these obstacles.

In this project's scope, the electrode position and body shape identification are related inasmuch as thoracic EIT instrumentation imposes geometric constraints of construction. It means that these two variables might be solved by computing the curvature of the tape segment between electrodes. Although contact impedance estimation is also significant to the improvement of images, it is not part of this project's intentions.

Regarding that, some already used approaches that could be useful to support body curvature and electrode position in EIT are presented in chapter 2.

1.3 Expected results

The concept to be approached is one that uses an additional device attached to the belt to estimate the boundary contour of the body dissociated from image reconstruction itself. This project attempts to:

- develop of an electronic device able to sense the bending displacement along the existing EIT electrodes belt, and
- propose a mathematical method capable to reconstruct 2-dimensions curves from bending displacement measurements.

Considering the physical aspects of electrodes belt used and ICU setting, and the actual state-of-the-art described in chapter 2, the strain gauge approach seems to be most suitable to requirements of biocompatibility, small size, low invasibility, accuracy and result consistency. Additionally, strain gage is a widespread technology, fact that increases the feasibility and applicability in clinical cases.

Investigations regarding the accomplishment of requirements for clinical use and the effectiveness of measuring body shape in EIT context are contemplated in this thesis's proposition. For this purpose, execution and experimentation of electronic circuit and mathematical simulations for the reconstruction method are schemed.

2 STATE-OF-THE-ART

Anthropometry stands for study of individual human body measurements aiming to quantify physical variations. Information about body size and shape is currently used by different study fields such as biological and medical statistics, forensic medicine and ergonomics.

Along the last century, as the understanding of human dimensions has been improved, the anthropometry techniques have also advanced. The first and simplest measurements were done manually using dedicated instruments like tapes, clipers, stadiometers, goniometers, etc (NORTON; OLDS, 1996).

During the 1970s and 1980s, however, novel principles of measurements started being developed primarily focusing in the mechanical manufacturing industry, for measurement and quality control, and gradually appearing in anthropometric applications whether to improve existing ones or to develop new ones. The progress is mainly due to electronics advancement in sensor-mechanical integration, optical components and image capturing and processing, as well as in computer science and technology.

Below are described recent methods used to estimate body shape, their uses, as well as possible advantages and disadvantages in this project, building foundation of its development.

2.1 Simultaneous reconstruction method

One trend of solving the problem of body shape and electrode position identification is not by introducing any further device but by means of EIT measurements information, i.e., using the same data needed to reconstruct image to extract the body shape.

The most common way to generate images without a precise boundary shape definition is by means of *difference imaging* technique in which the admittivity distribution is reconstructed by the difference between EIT

measurements in two different time instants or frequencies (BARBER; BROWN, 1984). However, the method assumes that the modeling errors are removed when the operation is done, relying on the linear approximation of a highly non-linear forward model of EIT. Moreover, this estimation is under the hypothesis of invariability of boundary shape between two measurements, which is not compatible to the thorax imaging scenario during breathing cycles.

Recent studies introduce interactive Newton-type least squares algorithms that uses *absolute images* to estimate the shape of the object boundary as part of the reconstruction process. This method is called *Simultaneous reconstruction of outer boundary shape and admittivity distribution* and was proposed by Dardé et al. (2013b).

For the shape differentiation, the *complete electrode model* (CEM) is used, which takes into account electrode shapes and contact impedance at electrode-object interface (CHENG et al., 1989). Through domain derivatives techniques, Fréchet derivation of the measurement map of the Complete Electrode Model (CEM) with respect to the exterior boundary shape is computed.

The newness of this approach comes up with a different method for sampling the regular shape derivative, overcoming issues with the derived definition and making it computationally more tractable. Therefore, the reconstruction algorithm can be implemented without having to solve forward problems with boundary conditions. Additionally, by numerical examples, the method was able to demonstrate that EIT measurements carry information not only on the admittivity distribution but also on the object's boundary shape.

Although the technique provides reasonable reconstructions even if substantially misspecified geometry, as seen in figure 2.1, the computation of a single image by full use of the algorithm takes on average 10 minutes to be generated with four Intel Core i7 processors with clock speed 2.3 GHz. It requires two steps to reduce the instability of contact impedances: the first for shape boundary reconstruction which evolves constant remeshing of the computational domain, and the second for contact impedances treatment

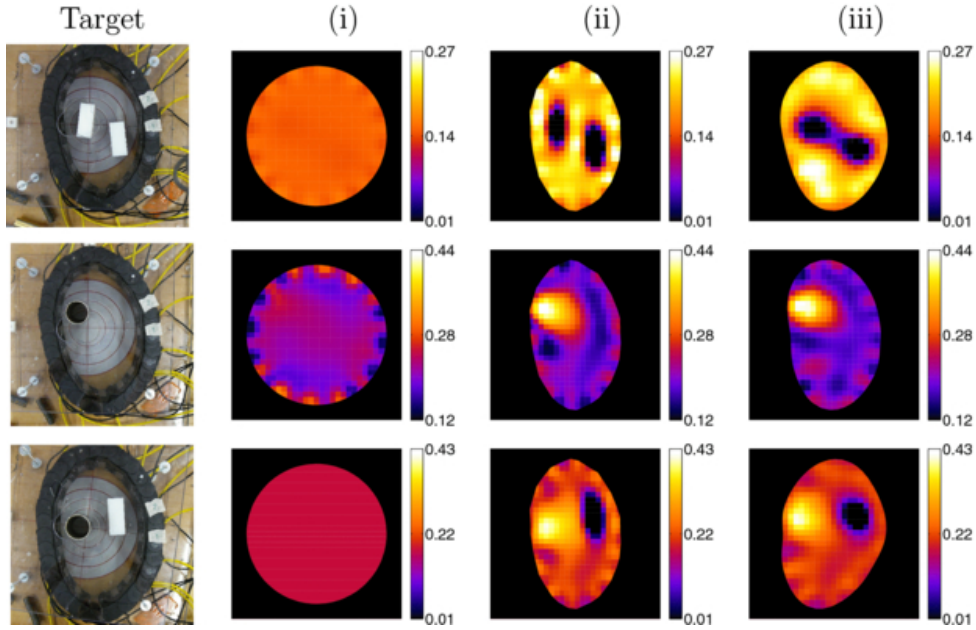


Figure 2.1 – One of experimental evaluation results extracted from [Dardé et al. \(2013a\)](#). First column: photos of the targets (top: two plastic cuboids; middle: a hollow steel cylinder; bottom: a hollow steel cylinder and a plastic cuboid). Second column: reconstructions with an incorrect geometry. Third column: reconstructions with an (almost) accurate geometry. Fourth column: simultaneous reconstructions of the geometry and the conductivity by the full algorithm.

([DARDÉ et al., 2013a](#)).

Nevertheless, as previously mentioned in section 1.1, the main applications of EIT are in ICU procedures which means there is needfulness of fast responses.

As it is possible to see in figure 2.1 case (iii), inaccuracy of water tank shapes stems from the compensation of smoothing requirements for admittivity estimation, i.e., final boundary shapes suffers from the compensation of excessively rounded phantom's image. As proposed in the validation of the method, case (ii), *a priori* information of the body shape would tackle this unwanted phenomenon, improving the initial guess and potentially allowing integration of redundant data from different strategy measurements.


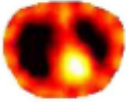
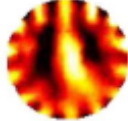
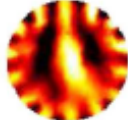
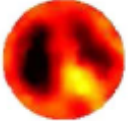
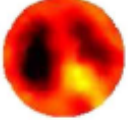
2.2 Compensation of modelling errors

Another proposal to reduce the effects body shape inaccuracy in the EIT imaging reconstruction process for *absolute imaging* technique is to compensate approximation errors by means of statistical tools. According to [Nissinen et al. \(2011\)](#), it is possible to use the Bayesian approximation error approach to represent not only the measurement error, but also the effects of the computational model errors and uncertainties as an auxiliary additive noise process in the observation model.

In this context, the realization of the modeling error, which is unknown since its value depends on the actual unknown conductivity and body shape, is statistically estimated over the prior distribution models of the conductivity and the parameterization of the body shape. The approximation error statistics are then used in the reconstruction process to compensate for the inaccurately known body shape ([NISSINEN et al., 2011](#)).

One of the evaluations the approach is submitted to simulation with a 3-D example with experimental data from a thorax shaped measurement tank the simulation, considering different prior models and the approximation error statistics is computed likewise each of them. From figure 2.2, MAP-CEM refers to *maximum a posteriori estimation with conventional error model*, while MAP-AEM is *maximum a posteriori estimation with approximation error model*. Each reconstruction model is derived considering different domain model. $U_\sigma(\tilde{\sigma}, \gamma)$ is the correct domain, $U_\sigma(\sigma, \tilde{\gamma})$ is the model domain using fine discretization and $U_h(\sigma, \tilde{\gamma})$ is the model domain using coarse discretization.

The results show that the reconstruction errors caused by the inaccurately known body shape can be reduced by employing the approximation error approach ([NISSINEN et al., 2011](#)). Relative estimation error is considerably low when correct domain is applied, although the simultaneous treatment of the modeling errors caused by unknown body shape and coarse discretization of the forward model is feasible, allowing the use of computationally efficient reduced order models.

Estimate	Forward model	Reconstruction	N_n	CPU time
EIT phantom Lungs = 0.73 mS cm^{-1} Background = 3.0 mS cm^{-1} Heart = 5.8 mS cm^{-1}				
MAP-CEM	$U_\delta(\bar{\sigma}, \gamma)$		23949	307 s
MAP-CEM	$U_\delta(\sigma, \bar{\gamma})$		16401	384 s
MAP-CEM	$U_h(\sigma, \bar{\gamma})$		1283	65 s
MAP-AEM	$U_\delta(\sigma, \bar{\gamma})$		16401	383 s
MAP-AEM	$U_h(\sigma, \bar{\gamma})$		1283	65 s




Figure 2.2 – 3-D example of compensation error modeling method with experimental data from a thorax shaped measurement tank taken from (NISSINEN et al., 2011). The measurement phantom and MAP estimates with real data. The images show the central horizontal cross sections from the 3-D reconstructions. N_n is the number of nodes in the forward mesh.

However, it is discussed the improvements to the compensation error modeling method if other imaging method are used to obtain initial domain information for reconstruction. Nissinen et al. (2011) affirms that When applying the approach to imaging of human chest, a more realistic approximation for the error statistics could be obtained if one has access to ensemble of 3-D chest CT (or MRI) images.

2.3 Computer vision

Computational vision is an interdisciplinary field in artificial intelligence, accountable for the acquisition, processing and analysis of visual information to develop image understanding systems, which automatize the scene description from image input data.

Its bases, developed in 1970s, are currently used in a wide variety of applications, such as: optical character recognition (OCR), machine inspection, retail, 3D model building, medical imaging, automotive safety, match move, motion capture, surveillance and biometrics (SZELISKI, 2010).

From anthropometric viewpoint, computer vision might deliver benefits with respect to conventional methods as it suffers less from operator variability, it is more adaptable to different environments, with low invasibility into the activity, besides presenting equally accurate results.

Therefore, image analysis handles transformation operations to transpose real world measurements into image virtual space to extraction of quantitative information from images. In fact, this superimposition is a critical and a constantly improved issue in image registration process to not lose accuracy and to well reproduce real data.

Toward applicability of vision-based three-dimensional reconstruction system with measurement proposes, there exist some common issues to be solved before applying any of current available methods:

Camera pose position of the camera with respect to an absolute reference system or, in specific cases, with respect to a pre-calibrated reference mounted on entire device. This parameter provides information about viewpoints and scene distances. Moreover, there are intrinsic camera specifications to be taken into consideration which defines image reference with respect to physical camera system.

Patient pose position of the patient/target with respect to absolute reference system or, in specific cases, to a pre-calibrated system of camera device. The superimposition of 3D points in space operates on both

patient, camera and image references written in a common reference system (absolute or pre-calibrated).

Transformation operator comparison operation between patient, camera and image references. There exist many ways to accomplish this task choosing which simplifications or hypothesis are possible to be used in each case. Some examples are roto-translation transformation, considering just rotation and translation between references, affine transformation, including scale and perspective, deformable transformation, studying body elastical changes or optical deformities.

Feature extraction extraction of useful information from an image. Once the relation between virtual and real world is known, the following step is the identification of interesting structures within the image. Automatic extraction strategies are many (e.g., edge detection, contours detection, region classification, etc), however, in medical purposes, a final professional evaluation is still needed.

Modeling constrains of human body. Often it is not possible to provide visual data from entire body, hence it is almost inevitable the construction of a body model that imposes basic shapes, anatomical and physical constrains. Measurements provided from previous steps are superimposed to the model.

Although such challenges are present in basically any system of human modeling, many solutions are coming up in market, in medical and anthropometric applications. Systems and studies detailed in the following subsections adopt computer vision principles to realize the reconstruction or tracking tasks of human body.

2.3.1 Optical Localizers

State-of-the-art in Computer Aided Surgery (CAS) applications, optical localization technique stands out for reaching high levels of accuracy and precision. In anthropometry it is significantly used in posture, motion and structure valuations of athletes and disabled people. It is also used in

entertainment, as in film industry, to recreate animation movements with motion capture systems (MOCAP).



(a) MOCAP actor from [Brown \(2017\)](#) (b) Sport movement valuation from [Noiumkar e Tirakoat \(2013\)](#)

Figure 2.3 – Application of optical markers in (a) entertainment and (b) sports medicine.

In most common clinical applications, the system is composed by:

Cameras at least two different perspectives of the scene are expected to 3D reconstruction. In medical applications, infra-red (IR) cameras are often employed.

Markers small objects able to reflect or emit light. The active ones are made with Light Emitting Diode (LED) flashing in a certain frequency. The passive ones are covered by reflective material of a specific spectrum exposed to light flashes (usually IR).

To capture the points in space, the cameras are set in the scene and markers are attached to the body. The cameras, then, capture the light reflected or emitted from markers and imaging algorithms are applied to accomplish the tasks of: (a) identification of markers in the image (b) correlation of markers identified in each image at a given time (c) transformation into real world coordinates (d) correlation in time of each marker among images.

Systems presented in the market can be divided into two main categories: absolute systems and pre-calibrated systems. Absolute systems are set with respect to an absolute reference which data is written on, for that reason it is necessary to calibrate cameras position with respect to

rooms reference at each utilization. Pre-calibrated systems, instead, intend to write spatial data over the reference system of the optical device, i.e, camera relative positions are fixed and a coordinate system is constructed and calibrated by the producer, as seen in figure 2.4 from ([Northern Digital Inc., 2017](#)).

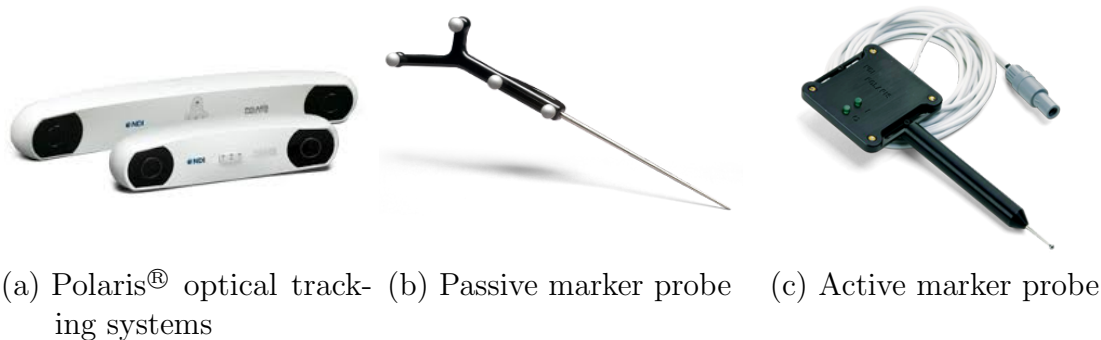


Figure 2.4 – Optical measurement systems from ©2017 Northern Digital Inc..Images taken from ([Northern Digital Inc., 2017](#))

Markers attachment position is a fundamental key in the process as it should be correspondent to one known body position. One possible approach to locate them is to refer to visible anatomical structures, such as bone terminations and prominent extremities, to match markers instant positions with respect to reference models. OpenSim from National Center for Simulation in Rehabilitation Research (NCSRR), for example, is an open source software system that allows building and analyzing musculoskeletal models and dynamic simulations of movement with data acquired from optical measurements ([DELP et al., 2007](#)).

Another technique, mainly used in stereotactic procedures, is to perform a patient image by means of medical imaging devices, as CT and MRI, to construct an individual model of patient having the markers already attached. These markers must be visible in two situations, during imaging exams and during optical tracker. Thereafter, when executing tracking procedure, points captured during tracker are superimposed to initial patient model.

These two approaches present advantages and disadvantages. The first method has easy applicability and is totally non-invasive, but its results are strongly dependent on the operator's manual ability to locate

strategic points. The second one, although it achieves greater accuracy levels considering specific body models, is invasive since subject cannot take off markers from modeling and tracking phases. Moreover, stereotactic approach considers the hypothesis of body rigidity, i.e., assumes that there are no changes between two phases. Besides, both techniques undergo problems with slip motion between skin and intern structure due to soft tissue mechanical properties.

Particularly to this project's scope, optical systems to body shape and electrode position identification may not be applicable, as in ICU environment there are plenty of objects in the scene, demanding complex feature extraction procedure. Beyond that, in ICU, it is hard to avoid occlusion situations, that is, cameras field of view are not guaranteed, and in long term analysis as EIT proposes, the rigidity of the patients body or the fit with anatomical maps diminish optical systems applications in this field.

2.3.2 3D scanning

Markerless image-based method is another solution for human modeling. Although the state-of-the-art multi-view stereo (MVS) and Structure from Motion (SFM) has produced desirable results, in particular accurate camera tracking and sparse reconstructions (AGUIAR et al., 2008; FITZGIBBON; ZISSERMAN, 1998), and increasingly reconstruction of dense surfaces (SEITZ et al., 2006), these methods are computationally heavy and not feasible to real-time applications.

That is the motivation of depth cameras such as Microsoft Kinect have attracted much attention in the community recently for 3D scanning (e.g. (TONG et al., 2012) and (HENRY et al., 2012)). Notably, Kinect is a new and widely-available commodity sensor platform that incorporates a structured light based depth sensor. Using an on-board ASIC an 11-bit 640x480 depth map is generated at 30Hz (NEWCOMBE et al., 2011).

Despite the significant cost-quality ratio of Kinect's depth map, the images contain numerous chasms where structured light depth is not read.

This can be due to materials or scene structures which do not reflect IR light, very thin structures or surfaces at glancing incidence angles.

To overcome this weakness, [Newcombe et al. \(2011\)](#) proposed an integration of Kinect and commodity graphics hardware (GPU hardware) to create a system for accurate real-time volumetric reconstruction of complex and arbitrary indoor scenes. The main concept uses a handheld Kinect depth sensor, which can be simply moved by users to generate a continuously updating, smooth, fully fused 3D surface reconstruction. The innovation of this work is the capability to continuously track the 6 degrees-of-freedom pose of the sensor using all of the live data available from it, rather than a feature subset, allowing to integrate depth measurements into a global dense volumetric model. The results of their work is shown in figure 2.5.

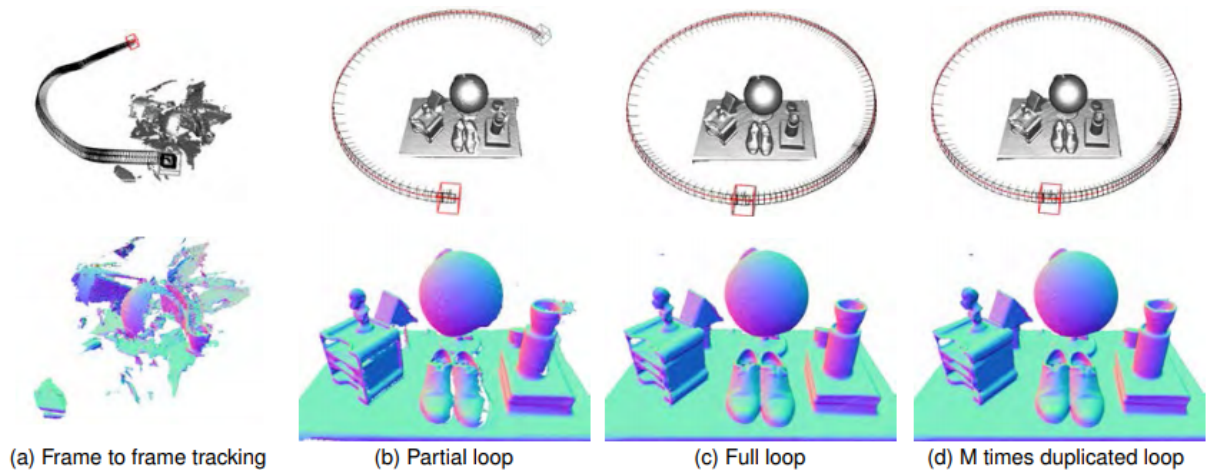


Figure 2.5 – Extracted from ([NEWCOMBE et al., 2011](#)). Results from circular motion experiences. For each column, the top row shows the estimated sensor trajectory and the bottom row reconstruction view. (a) Frame-to-frame tracking, where the pose of each new frame is estimated by registration against just the last frame. Poor reconstruction due to non-circular trajectory. (b) Processing is halted with the loop two-thirds complete. (c) shows loop closure, where the last frame processed is a duplication of the first frame. (d) same data from (c) and taken repeatedly.

Notwithstanding promising results in many fields, the procedure could partially solve body shape and electrode position in EIT. While in ICU, patients are set lying on the stretcher with monitoring devices, restricting

his or her mobility. For that reason, circling around the patient is scarcely possible in less than half of a loop complete. Besides that, certain static structure around the patient is required which decreases even more patient's mobility and hinders medical access to him or her.

2.4 Optical fiber

The sensitivity of untreated optical fibers is insufficient to detect the deformation of structures in bending. Techniques to enhance sensitivity are focused on the creation of a sensitive zone over one side of the fiber. Consequently, it is possible to sense that the ray propagation path concentrates to the convex side of bent fiber, as the number of reflections is increased in the convex side and reduced in the concave side.

Advantages such as biocompatibility, wide bandwidth, and small size have led optical fiber sensors to be used in different biomedical applications. Studies about the relevance of this sensor to determine diaphragm curvature (LAWSON; TEKIPPE, 1983), as well as to monitor cardiac and respiratory movement (SILVA et al., 2011) and specific sensors for MRI applications, as optical fiber does not have significant behavior changes under high magnetic field (TAFFONI et al., 2013).

However, sensors might have limited long-term stability due to emission sources variations, which induces errors in measurements and limits resolution. Sensor coupling in order to extend its sensing field and temperature variations also have consequences in accuracy of system. Other disadvantage is that if there is constant presence of water vapor in atmosphere, the device will have a slow replacement of deuterium by hydrogen atoms decreasing its shelf-life.

2.5 Strain gauge

When a fine wire is strained within its elastic limit, the wire's resistance changes because of changes in the diameter, length and resistivity. The resulting strain gauges may be used to measure extremely small displace-

ments. Displacement sensors can be in both direct or indirect systems of measurements of size, shape and position of organs and tissues in the body.

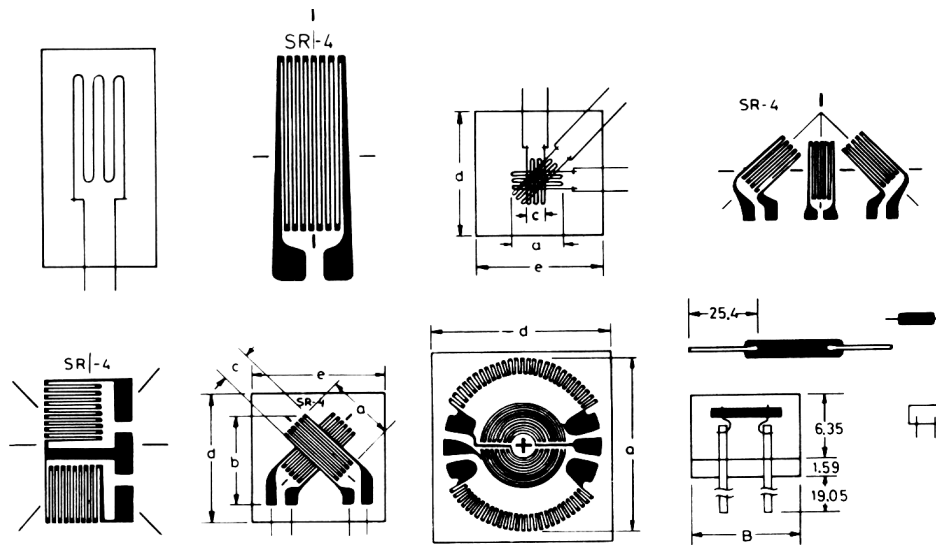


Figure 2.6 – Several bounded and unbounded metal and semiconductor strain gauges (from BHL electronics)

Strain gauges are a well-known practice in generic engineering processes. Whereas the strain gage's adaptability contributed to its widespread use in the field of experimental stress analysis, it was the high degree of measurement accuracy that could be obtained which made the strain gage attractive for transducer manufacture. Both wound wire and foil types produce strain gauges which are known as metal strain gauges due to their metal alloy measuring grids ([HOFFMANN, 1989](#)).

In medical application, sensor is customized to attempt its use in non-critical and critical medical device and equipment applications. It is widely applied in functional valuation of joints, as electrogoniometers for angular displacement, in cardiovascular and respiratory dimensional and plethysmographic determinations ([WEBSTER, 1978](#)). Its flexibility of use is partially explained by the varied configurations it can assume, revealing strains in multiple directions and different conditions, as it is possible to see in figure 2.6.

In imaging technologies, multi-axis strain gages sub-assembly are commonly used in CT Scan Machines to guarantee smooth reliable movement and table positioning for different weight distribution when positioning pa-

tient inside scanning tube, demanding high performance. In mammography machines, dual or triaxial strain gages are used to monitor the amount of physical effort is applied to patient by the machine during imaging capture.

Customized strain gage sensors are often used in remote robotics surgeries. The equipment demands sensors to precisely measure depth of force and drill bit rotational force during remote hip surgeries. For that reason, strain gages are developed to identify both tension and compression to measure downward and upward force and motion. Additionally, some applications expect sensors to measure full deflection and drilling motion consistency, ensuring reliable patient positioning on the operating table.

Determination of body shape using strain gauges has been done for many specific applications. [Oliveira \(2015\)](#) experimented a strain gauge configuration able to characterize curvature of cylindrical shapes to be used in ultrasound applications. In [Yi et al. \(2010\)](#), strain gauges are used in endoscopy devices to reconstruct the shape of flexible rod by means of strain information.

The applicability in this project scope is encouraging considering low invasibility this device brings to ICU scenario as result of its small dimensions. Moreover, it is sourced by low voltages and currents that would bring no risk to patient and to EIT system and at the same time, the device is able to provide accurate measures even with small displacements. Low costs and accessibility of the sensor are also advantages to be considered.

3 MATERIALS AND METHODS

The developed system that enables body shape and consequently electrode positioning identification is a close conjunction between an electronic measurement device and a curve reconstruction method described in sections 3.1 and 3.2, respectively. Additionally, the chapter presents the simulation procedure (section 3.3) and the evaluation methods (section 3.4) used to appraise system's results.

3.1 Shape identification device

From discussion presented in chapter 1, the electronic device is built around strain gauge technology, furnishing information to a mathematical method able to estimate curvature.

3.1.1 Belt configuration

Electrode distribution around the body is a key issue to EIT systems. A belt structure, where electrodes are assembled, has been designed for fostering the use on recumbent patients in supine, lateral or prone position, as shown in figure 3.1. The only belt position remark is one reference electrode supposed to be attached to a central point on the body ([TESCHNER et al., 2010](#)).

Usually, the supporting band is composed by non-conductive materials which have also a cushioning effect, such as silicone. Due to complex cable systems around electrodes, EIT belt system may vary from 50 mm to 100 mm thick and at least 40 mm wide.

As an additive feature, the shape identification device is expected to be independent and suitable to already existing EIT imaging technologies. The schemed solution aims to measure flexing displacements that occur when EIT belt envelops the patient's body circumference. Using strain gauge sensors, besides uniaxial deformations, makes it also possible to sense



(a) EIT electrode belt configuration (b) EIT belt for respiratory ventilation monitoring in intensive care patients

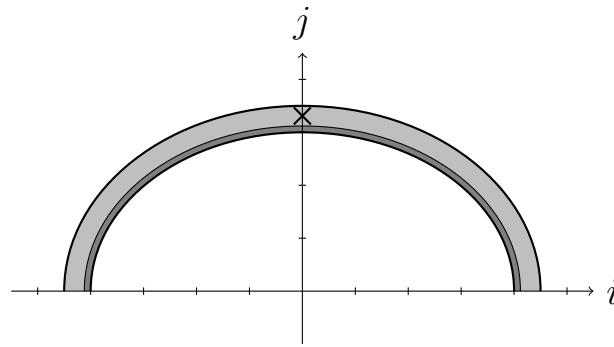
Figure 3.1 – (a) and (b) belong to EIT system PulmoVista 500 from Drägerwerk AG & Co. KGaA. The belt contains 16 electrodes placed around the chest wall with circumference varying from 70 cm to 150 cm. Taken from (TESCHNER et al., 2010).

strain due to bending when properly disposed over the sample (see figure 3.6).

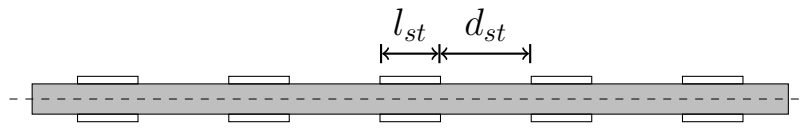
Therefore, a sunder sensitive belt was designed to have strain gauge sensors affixed over a backing (figure 3.1b), with diminished total thickness that does not interfere with EIT belt dimensions. It has been conceived as a thin layer located preferably nearby to the patient skin represented by disposal schematic in figure 3.2a.

Additionally, backing material was selected to be non-conductive, flexible and to have low elasticity to a better sensors' packing. As in figure 3.2b, strain gauges are arranged on both belt sides to measure deflection of middle reference line confronting compressive and tensile stress.

Sensing segments provide discrete measurements about belt's deflection since along distance d_{st} , indicated in figure 3.2b, there is no available information. For that reason, d_{st} is a constrain parameter to be defined by a convenient reconstruction method described in section 3.2.



- (a) Schematic representation of half of a human body dressed with EIT belt (light gray) and sensing belt layer (dark gray). Black cross is the reference electrode position on central point of abdomen.



- (b) Diagram of sensing belt in flat position. Backing material is represented by light gray structure bisected by dashed reference line. Strain gauges (white rectangles) are glued above and below the belt. Sensing segment is defined as a pair of aligned sensors across both sides of the belt. l_{st} is sensor's active length and d_{st} is the distance between consecutive sensors.

Figure 3.2 – Device model: (a) highlights system's application inside existing EIT belts while (b) illustrates sensing belt architecture.

3.1.2 Strain gauge

Strain is the amount of deformation of a body due to an applied force. Strain, ϵ , is defined as fractional change in length and can be positive (tensile) or negative (compressive).

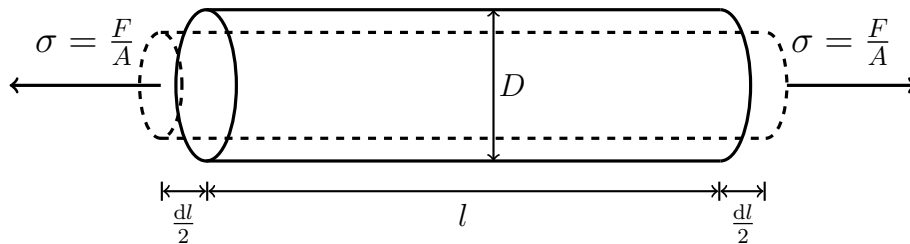


Figure 3.3 – When bar strain is the effect of an uniaxial force, there is a change of length l of material proportional to cross sectional area, A , and to an applied force, F .

Strain gauge is a resistive sensor able to measure extremely small displacements, on the order of nanometers, from resistance variation due to changes in its geometry. This phenomenon occurs when a fine wire is

strained within its elastic limit and, therefore, is described by Hooke's law:

$$\sigma = \frac{F}{A} = E\epsilon = E\frac{dl}{l} \quad (3.1)$$

E is Young's modulus, σ is the applied stress and ϵ is the dimensional strain. That means strain should not exceed 4% of gauge length which is, approximately, 50 000 m ϵ for metal gauges.

However, when a bar is strained, a phenomenon known as *Poisson Strain* causes the contraction in transverse direction of the girth of the bar, D . Poisson's Ratio, ν , of a material is the proportion between the strain in transverse direction (perpendicular to the force) to the strain in axial direction (parallel to the force) that defines Poisson effect:

$$\nu = -\frac{dD/D}{dl/l} \quad (3.2)$$

For most metals, Poisson's ratio, ν , ranges from 0.20 to 0.35.

Considering sensor's material structure homogeneous, it is conceivable to define electrical resistance R as function of its dimensions and resistivity which is represented by derivative equation 3.3 below, depending on resistivity ρ , longitudinal length l and cross sectional area A .

$$\frac{dR}{R} = \frac{dl}{l} - \frac{dA}{A} + \frac{d\rho}{\rho} \quad (3.3)$$

Gauge factor, G , is the ratio of relative change in resistance to relative change in length (strain). From equation 3.3 is possible to obtain:

$$G = \frac{dR/R}{dl/l} = 1 - \frac{dA/A}{dl/l} + \frac{d\rho/\rho}{dl/l} \quad (3.4)$$

First term of equation 3.4 is representative of variation in resistance caused by structure strain. The second term is the contribution to resistance change of the cross-sectional area variation which, in turn, is correlated to length variation by Poisson effect, defined in equation 3.2. The last term expresses variation of resistivity due to mechanical stress, also known as piezoresistive effect.

In metallic material, piezoresistive effect is experienced as a result of alteration in vibration amplitude of its atoms. Longitudinal stress, as in figure 3.3, raises vibrations that consequently reduce electronic mobility and increases material's resistivity.

In metals, percentage variations of resistivity and volume are proportional to Bridgman's constant C :

$$\frac{d\rho}{\rho} = C \frac{dV}{V} \quad (3.5)$$

Bridgman's constant ranges, in usual alloys, from 1.13 to 1.15.

Therefore, assuming hypothesis of cylindrical structure, isotropic material within elastic limit, equation 3.4 is rearranged to

$$G = \frac{dR/R}{dl/l} = 1 + 2\nu + C(1 - 2\nu) \quad (3.6)$$

For the scope of this project, were used strain gauges model PA-06-250BA-120 schematically represented by figure 3.4. The device consists of very fine wire or metallic foil arranged in a grid pattern to maximize the amount of metallic wire or foil subject to strain in parallel direction. The cross sectional area of the grid is minimized to reduce *Poisson Strain* effect and shear strain.

For that reason, it is possible to consider negligible Poisson ratio, ν , in equation 3.6. Moreover, the grid is bonded to a thin backing, called the carrier, which is attached directly to the test specimen. Therefore, the strain experienced by the sample is transferred directly to the strain gauge, which responds with enough linear change in electrical resistance for small variations.

$$R = R_0 + dR = R_0 \left(1 + \frac{dR}{R_0}\right) \approx R_0(1 + G\epsilon) \quad (3.7)$$

Ideally, resistance of the strain gauge changes only in response to applied strain. However, strain gauge material, as well as the specimen

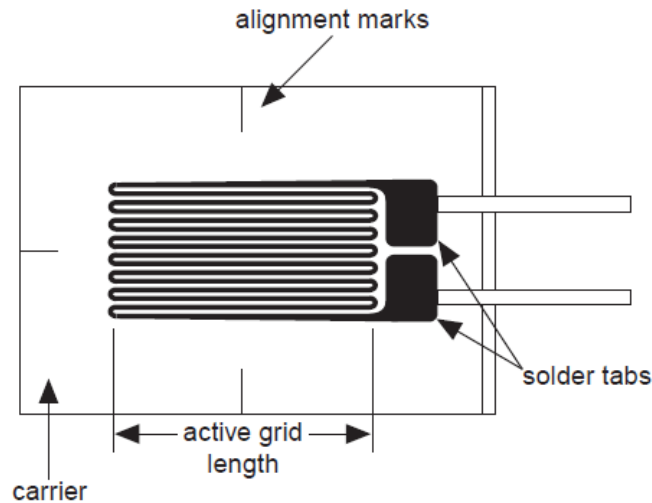


Figure 3.4 – Bonded Metallic Strain Gauge - most widely used gauge. Extracted from [National Instruments \(1998\)](#)

Table 3.1 – Data-sheet relevant information for strain gauge model PA-06-250BA-120 provided by Excel Sensores IND. COM. EXPORT.LTDA

Characteristic	Value	Unit
Carrier Material	laminated polyamide	-
Carrier Dimensions	9.47×3.18	mm
Active Grid Material	55% nickel 45% copper	-
Active Grid Dimensions	6.35×3.18	mm
Electrical Resistance	120 ± 0.5	Ω
Gauge Factor	$2.11 \pm 1\%$	-
Maximal Deformation	$\pm 3\%$	-

material to which the gauge is applied, will also respond to changes in temperature.

Temperature variations derive from external source of heating but also from self-heating effect. As resistance measurement implies on passing an electric current through it, the greater is the voltage/current supply, greater is the power dissipation in thermal form. Strain gauge manufacturers attempt to minimize the effect limiting maximal current is $25 \mu\text{A}$ for metal gauges that are good heat conductors such as steel, copper, aluminum, magnesium and titanium ones. According to sensor datasheet, temperature self-compensation follows the steel behavior, as shown in table 3.2.

Table 3.2 – Temperature self-compensation behavior for strain gauge model PA-06-250BA-120 provided by Excel Sensores IND. COM. EXPORT. LTDA

Temperature (°C)	Deformation ($\mu\epsilon$)
0	-45
10	-10
20	-5
30	+15
40	+13
50	+5

As described in chapter 1, the methodology for curvature identification and electrode positioning must be suitable for ICU conditions, which means it is appropriate to consider temperature ranging from 30 °C to 40 °C.

3.1.3 Electronic circuit

In practice, the strain measurements rarely involves quantities larger than a few millistrain ($\epsilon \times 10^{-3}$). Therefore, to measure the strain requires accuracy for very small changes in resistance.

Wheatstone bridge configuration permits to measure small resistances based on a feedback system, either electric or manual, in order to adjust the value of a standard resistor. Wheatstone bridges are often used in the deflection mode. Instead of measuring the action needed to restore balance on the bridge, this method measures the voltage difference between both voltage dividers or the current through a detector bridging them, as shown in figure 3.5.

Particularly for this project's scope, curvature determination is a result of belt material deflection. For that reason, the following derivations correspond to bridge configurations for flexural members.

As in figure 3.5, the full Wheatstone bridge is regularly used as conditioning circuit for strain gauges. The full bridge is composed by four identical strain gauges disposed in such a way that R_1 and R_3 have a positive strain while R_2 and R_4 have a negative strain for the same given

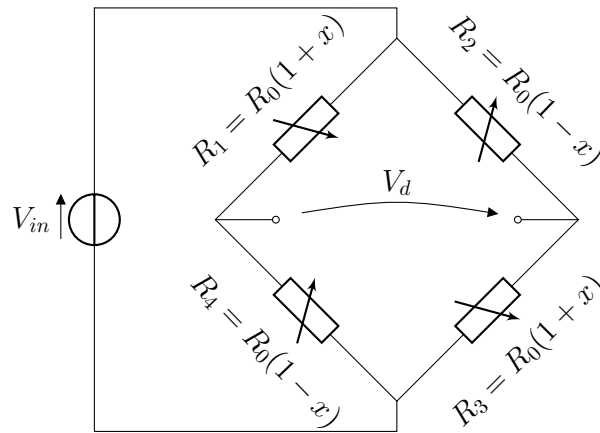


Figure 3.5 – Full Wheatstone bridge

deflection, as shown in figure 3.6.

The main advantage for the measurement circuit is the linearity. From equation 3.7, x corresponds to term $G\epsilon$. If the bridge is balanced when $x = 0$, which is usual the situation, and voltage source, V_{in} , is constant, voltage difference measured, V_d , is defined by

$$V_d = V_{in} \left(\frac{R_3}{R_2 + R_3} - \frac{R_4}{R_1 + R_4} \right) = V_{in} x \quad (3.8)$$

Linearity is not necessary to achieve good accuracy. However, if a proper positioning of strain gauges exists on sample, measurement accuracy is enhanced. In figure 3.6, is represented a scheme of bridge configuration for bending strain which brings important benefits for measuring: sensitivity to bending is maximized, axial strain is rejected and temperature is compensated.

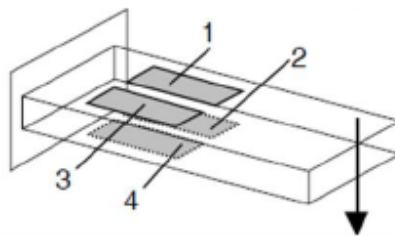


Figure 3.6 – Best bridge configuration for bending strain

Although improved with Wheatstone bridge, sensitivity can be increased by an amplifier stage. From equation 3.8, and knowing that for

metal strain gauges, x seldom exceeds 0.02, the variation of fluctuation of V_d will be barely noticed and easily corrupted by noise.

Signal conditioning is, thus, necessary for accuracy and repeatability of measurements. In figure 3.7 is represented a conditioning circuit using Instrumentation Amplifier (INA).

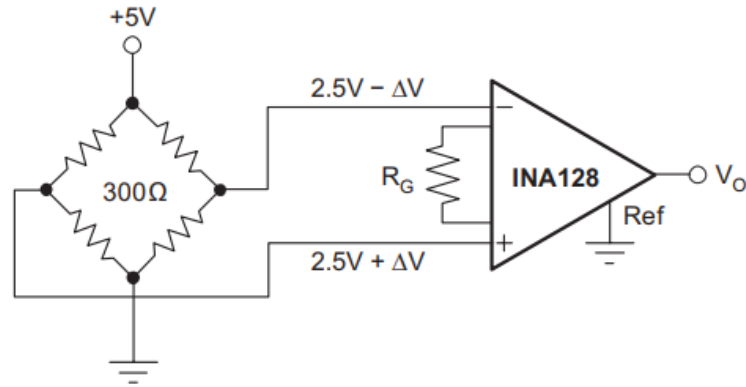


Figure 3.7 – Bridge amplifier scheme taken from [Burr-Brown Corporation \(1996\)](#)

INA is a low-power, general purpose instrumentation amplifier that offers great accuracy through versatile three-operational-amplifier design (figure 3.8) which is the preferred solution for applications of resistive sensors on bridge disposal ([TEXAS INSTRUMENT, 1995](#)). The device can be configured to monitor the input differential voltage with an adjustable gain. Besides, INA circuitry presents good common mode noise rejection and accurate linear behavior when symmetrically sourced with typical voltage value of ± 15 V.

Thence INA model 129PA from Burr-Brown Corporation producer was selected and is mathematically described by the following characteristic equations from ([TEXAS INSTRUMENT, 1995](#)):

$$V_0 = g \cdot (V_{in}^+ - V_{in}^-) \quad (3.9)$$

$$g = 1 + \frac{49.4 \text{ k}\Omega}{R_G} \quad (3.10)$$

V_0 is output signal referred to the output reference terminal (Ref in figure 3.8) which is grounded. V_{in}^+ and V_{in}^- are differential input signals. Gain, g , is set by connecting a single external resistor, R_G . In equation 3.10, $49.4\text{ k}\Omega$ constant comes from the sum of the two internal feedback resistors of A_1 and A_2 , in figure 3.8.

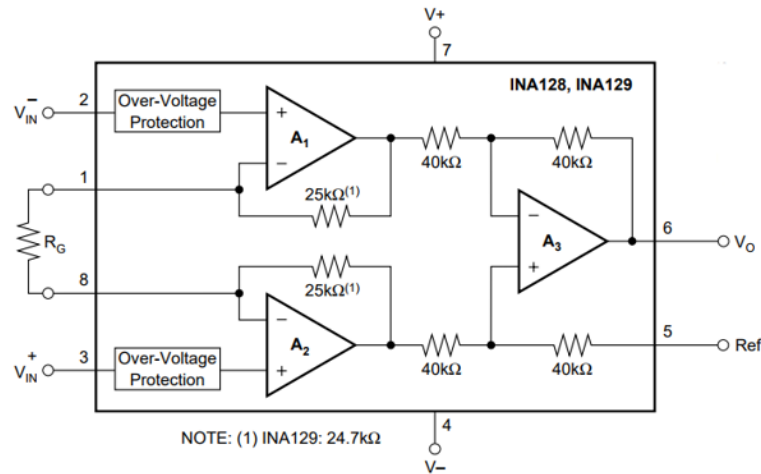


Figure 3.8 – Basic connections of INA129PA circuitry from [Burr-Brown Corporation \(1996\)](#)

Once strain gauge voltage is well-conditioned and amplified, output signal is processed by micro-controller before computationally treated. Arduino Mega 2560 is a micro-controller board based on ATmega2560 with facilities when programming the controller and communicating with a computer. Besides, it has 16 analog input pins with possible internal pull-up resistor of $20\text{ k}\Omega$ to $50\text{ k}\Omega$ operating at 5 V and of maximum current acceptance of 40 mA .

For each analog inputs, there is an Analog-to-Digital Converter (ADC) which resolution is 10 bits in a default voltage range of 0 V to 5 V ([ARDUINO, 2018](#)), not assuming negative input voltages. Nonetheless, INA129PA better performs when powered by a $\pm 15\text{ V}$ voltage source leading to output signal a fluctuation between much higher values than input maximum tension board admits.

To overcome that, it ought to limit output values of INA129PA by properly setting amplification gain and to employ a further conditioning circuitry after amplification phase. The final circuit, in figure 3.9, aimed to

shift signal range entirely to positive values within board voltage restriction.

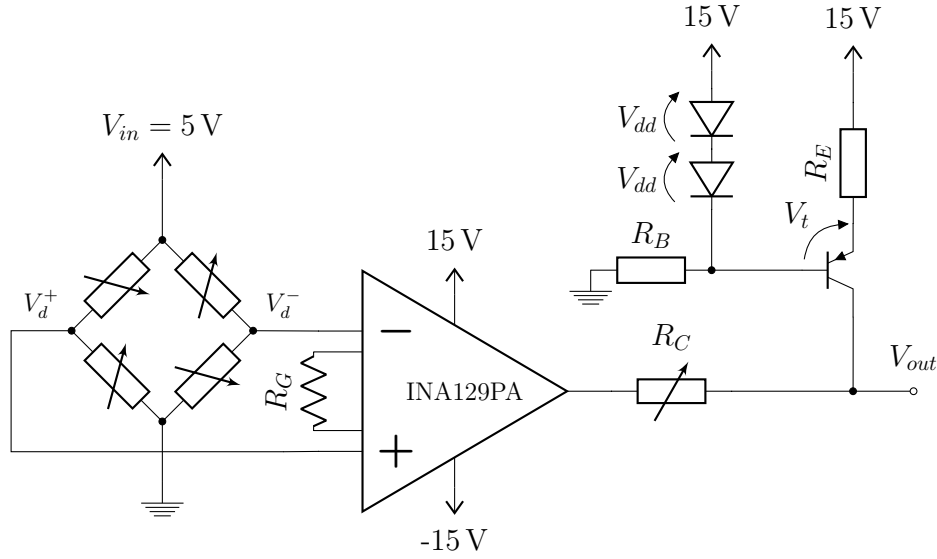


Figure 3.9 – Full conditioning circuit

R_G is arranged concerning V_0 , from equation 3.9, to range only between -2 V and 2 V . R_E and R_B attached to transistor ensure current to not go beyond INA129PA and Arduino maximal drive currents, that is lower than 1.5 mA . R_C is a variable resistor capable of implementing an accurate offset of 2.5 V .

From equations 3.8, 3.9, 3.10, the proposed conditioning circuit represented in figure 3.9, in a calibrated condition, presents a transfer function:

$$V_{out} = \left(1 + \frac{49.4\text{ k}\Omega}{R_G} \right) V_{in} G \epsilon + R_C \left(\frac{V_t - 2V_{dd}}{R_E} \right) \quad (3.11)$$

The resultant V_{out} signal is intended to vary between 0.5 V to 5 V , avoiding possible interference of boarder voltage values. When $V_{out} \in [0.5, 2.5[$, physical device is bent with negative concavity, when $V_{out} \in]2.5, 4.5]$, belt element is flexed with positive concavity. The neutral position (straight) is achieved when V_{out} is around 2.5 V .

3.1.4 Calibration procedure

An outcome of using strain gauge is the requirement of calibration scheme to reduce measurement errors. Calibration is branched out into the three steps

of conditioning circuit. Calibration components are trimming potentiometers with different nominal resistances capable to adjust measurement drifts of the system.

Bridge Balance Two potentiometers are displayed between strain gauge dividers to remove possible resistance discrepancies between sensors, balancing the full Wheatstone bridge. They have nominal resistances (R_t) comparable to the strain gauge one, in order to ensure that equation 3.8 terms in neutral flat position:

$$\frac{R_3 + y_t^+}{R_2 + R_3 + R_t} - \frac{R_4 + y_t^-}{R_1 + R_4 + R_t} = 0 \quad (3.12)$$

where y_t^+ and y_t^- are variable resistances of potentiometers of positive (V_d^+) and negative (V_d^-) bridge pins. The transfer function varies negligibly with respect to equation 3.11 provided that R_t is sufficiently small with respect to nominal resistance of strain gauges and sensors are limitedly strained.

Offset The fourth element ensures offset in V_{out} to be 2.5 V and is represented by variable resistor R_C in figure 3.9.

3.2 Curvature reconstruction method

Although measurement device, described in section 3.1, enables to extract strain, curvature is not directly quantified by it but is a result of a further mathematical modeling. Curve reconstruction method aims to generate continuous 2-dimensional curves using exclusively data from sensor device. Due to human thoracic anatomy, it must be guaranteed convex and concave curve reconstruction and relative position identification along estimated contour.

The estimation encompasses both sensitive and non-sensitive belt segments to enable continuity, meaning that mathematical model branches out into two steps:

Curvature modeling through parametric functions, silhouette of each sensing belt segment is estimated from strain measurement. The

approximation regards to strain gauges behavior and backing physical deflection.

Curve interpolation relative position between estimated curvature as well as approximation of non-sensitive gaps along belt occurs through a curve interpolation method that guarantees continuity of an unique contour line representing body boundary.

3.2.1 Curvature of the part of belt with strain gauges

The first phase of reconstructing body shape is to interpret scalar value from strain measurements into a 2-dimensional bend. The deflection displacement is understood as a result of a physical configuration based on strain gauge dimensions.

As represented in figures 3.2b and 3.6, strain gauges are placed in such a way to increase sensibility when measuring bending of the centered reference line. For each sensor is assigned an order number, n , with respect to its manufactured position. The first element is positioned besides the reference electrode of EIT belt, allowing electrode localization along the curve.

The computed strain regarded to the reference line is assumed bounded to a frame $\{F\}_n \in \mathbb{R}^2$ for a given sensing segment n . In flat calibrated position, center line segment is along i axis centered on $x = 0$, as in figure 3.10.

To accomplish modeling, each measured strain, ϵ_n , is defined as the fractional change in length between flat calibrated position, l_{st} , and final curve after bending deformation, l_n .

$$|\epsilon_n| = \frac{|l_n - l_{st}|}{l_{st}} \quad n = 1, 2 \dots N \quad (3.13)$$

N is the total number of sensing belt segments along the belt. Since ϵ_n results from a comparison between strain measurements above and below sensing belt, it refers to a dimensionless value with respect to the reference

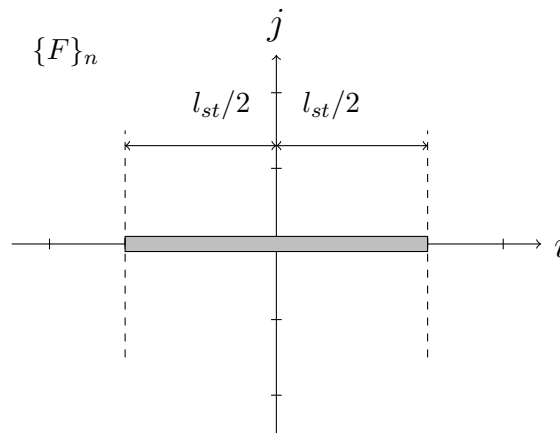


Figure 3.10 – Representation of flat calibrated position for a sensing belt segment. The light gray rectangle represents the sensing segment which is centered on its own frame n .

line. This determines final strain (equation 3.13) has to be always positive as it illustrates solely line elongation from bending phenomenon.

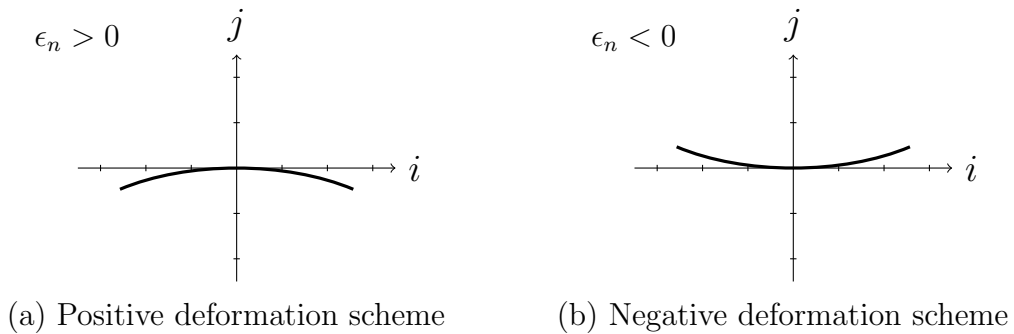


Figure 3.11 – Signal definition to represent curvature orientation according to sensing circuit arrangement

Deformation, however, is assigned to a signal indicative of curvature orientation that lands from circuit configuration described in section 3.1, shown in figure 3.9. As represented in figure 3.11, positive elongation means negative curvature while negative deformation means positive curvature of the curve.

Under such hypothesis, curvature is defined as a 2-dimensional vector function $\vec{\gamma}_n(t)$ that correlates i and j components to accomplish total length

equals to l_n :

$$\begin{aligned} \vec{\gamma}_n(t) &= (x(t), y(t)) && \text{such that,} \\ L &= \int_a^b \|\vec{\gamma}_n(t)\| dt = l_n \end{aligned} \quad (3.14)$$

Integration limits, a and b , are set symmetrically with respect to selected frame $\{F\}_n$. Assuming displacements are purely due to deflection, it is reasonable to consider no axial effort occurring and, therefore, no significant deformation in i direction.

Two studies about $\vec{\gamma}_n(t)$ are discussed in this thesis: parametrization of straight lines (subsection 3.2.1.1) and parametrization of circumference arcs (subsection 3.2.1.2). Through simulations of both strategies, it is verified their applicability to thoracic shape identification.

3.2.1.1 Linear approximation

Under linear approximation, reference line of sensing segment assumes a profile composed by symmetrical straight lines when bent. The deformation is a comparison between length in initial neutral state and length in final state, which is represented by absolute value function, as in figure 3.12.

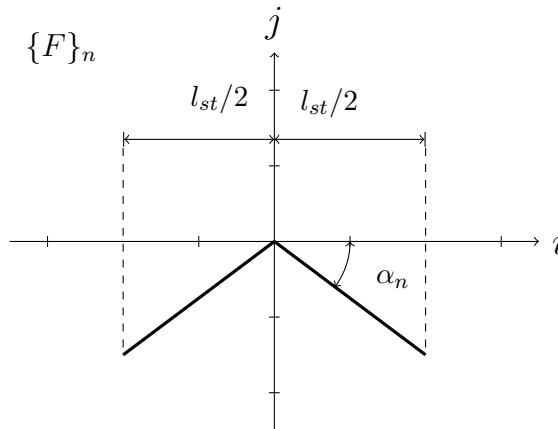


Figure 3.12 – Estimation of bending displacement of a sensing segment as straight lines profile.

The absolute value function is parameterized in two dimensions as in equation 3.15. Parametric variable, t , ranges symmetrically around j axis,

while α_n , between modeled line and i axis (figure 3.12), is assigned in first and fourth quadrants.

$$\begin{aligned} \vec{\gamma}_n(t) &= (t, \tan \alpha_n |t|) & -l_{st}/2 \leq t \leq l_{st}/2 & \quad \text{such that,} \\ l_n &= 2 l_{st} \sqrt{\sec \alpha_n^2} & -\frac{\pi}{2} < \alpha_n < \frac{\pi}{2} & \end{aligned} \quad (3.15)$$

As result of conditions above, it is possible to correlate the deformation of one sensible element, ϵ_n , with respect to angle α_n , as below:

$$\epsilon_n = \frac{1 - \cos \alpha_n}{\cos \alpha_n} \quad -\frac{\pi}{2} < \alpha_n < \frac{\pi}{2} \quad (3.16)$$

Linear approximation advantage lies on the low computational cost of equation 3.16, although presenting a significant lack of accuracy, tackled during simulation phase.

3.2.1.2 Circumference approximation

Under circumference approximation, sensor reference line is estimated through circumference parametrization when sensor is bent. The sensing segment profile is assumed as a circumference arc that has its symmetrical point on the origin of a given frame, $\{F\}_n$, and ranges in i direction around initial length symmetrically as in figure 3.13.

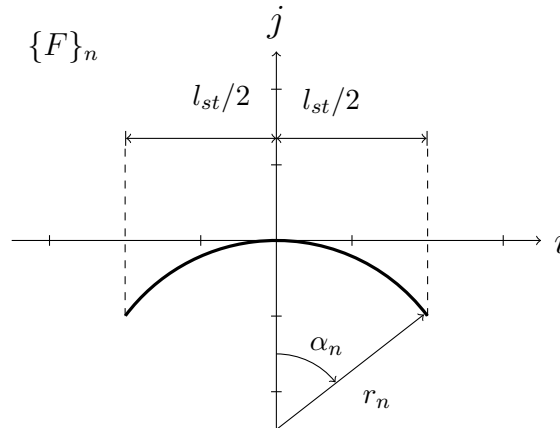


Figure 3.13 – Estimation of bending displacement of a sensing segment as circumference arc profile.

From equation 3.14, let $\vec{\gamma}_n(\alpha)$ be 2D parametric function that describes a circumference arc whose radius is r_n and amplitude angle α_n as in figure 3.13.

$$\begin{aligned} \vec{\gamma}_n(\alpha) &= (r_n \sin \alpha, r_n \cos \alpha - r_n) \quad 0 \leq |\alpha| \leq \alpha_n \quad \text{such that,} \\ l_n &= \int_{-\alpha_n}^{\alpha_n} \|\vec{\gamma}(\alpha)\| d\alpha = 2|\alpha_n| r_n \end{aligned} \quad (3.17)$$

It is defined a pair of equations that correlates ϵ_n to α_n and r_n , leading to a mismatched number of variables and equations. However, under the hypothesis of deflection displacements solely, another geometrical constrain is determined:

$$\vec{\gamma}_n(\alpha_n) = (l_{st}/2, y) \Rightarrow \sin \alpha_n = \frac{l_{st}}{2r_n} \quad (3.18)$$

From table 3.1, strain does not exceed 3% of typical length in typical applications, sustaining the assumption that α_n is sufficiently close to 0 to provide an accurate approximation of trigonometric function through series. Particularly, Taylor series represents functions as an infinite sum of terms that are calculated from functions' derivatives at a certain point. When centered at zero, Taylor series is called Maclaurin series, which is defined for sinus function as in equation 3.19.

$$\sin x = \sum_{n=0}^{\infty} \frac{(-1)^n}{(2n+1)!} x^{2n+1} \quad \text{for all } x \quad (3.19)$$

Therefore, joining equations 3.17, 3.18 and 3.19, variables r_n and α_n are obtained from ϵ_n .

$$\alpha_n = 2 \sqrt{\frac{5 + 5\epsilon_n - \sqrt{5(5 + 7\epsilon_n + 2\epsilon_n^2)}}{1 + \epsilon_n}} + \mathcal{O}(\alpha_n^7) \quad (3.20)$$

$$r_n = l_{st} \frac{1 + \epsilon_n}{2\alpha_n} + \mathcal{O}(\alpha_n^7) \quad (3.21)$$

Truncation of Maclaurin series in fifth order causes further errors than just mismatching from model, however, if $|\alpha_n| \ll 57^\circ$, truncation errors may be considered negligible.

3.2.2 Curvature of the part of belt between strain gauges

In body shape reconstruction method, curve interpolation is aimed to estimate lengths along belt whose strains are not measured. The absence of information in between two consecutive sensing pieces is an issue to curve continuity.

Although it is possible to decrease d_{st} (figure 3.2b) to negligible values, this implies the belt to have more than 600 sensors along it, considering sensors' dimensions presented in table 3.1. Curve interpolation is then an essential tool to enable viability and cost reduction of the sensing belt.

For N sensing segments equally distributed along the length of the belt in flat position, there are N frame references $\{F\}_n$. Each sensor curvature is estimated over its respectively frame, rather based on linear or circumference approximations. Initially, relative positions between sensing segments estimations are not known exactly.

The interpolation between consecutive sensor curvatures consists on (a) finding 2-dimensional curve to model the behavior of non-sensible segments (subsection 3.2.2.1) and (b) on evaluating relative position and orientation between sensors based on continuity constrains of the reconstructed curve (subsection 3.2.2.2).

3.2.2.1 Curvature interpolation model

An interpolation curve refers to an insensitive segment of the belt physically located in between two sensible segments. Equivalently to sensible segments, each interpolation curve is described in its own reference system called $\{B\}_m$.

m is the order number assigned to an insensitive segment that connects the n^{th} and $(n + 1)^{th}$ sensible segments with $n = m$. M total number of

insensitive belt pieces. When sensors are distributed along the whole belt, $M = N$.

Similarly to equations 3.14, the interpolation vector function, $\vec{\Gamma}_m(t)$, is defined for each non-sensible segments of the belt. $\vec{\Gamma}_m(t)$ is selected according to approximations chosen for sensors reference line estimation (subsections 3.2.1.1 and 3.2.1.2).

Linear interpolation $\vec{\Gamma}_m(t)$ is defined as a straight line that by simplicity is along i axis.

$$\vec{\Gamma}_m(t) = (t, 0) \quad -d_{st}/2 \leq t \leq d_{st}/2 \quad (3.22)$$

Mid-radius interpolation $\vec{\Gamma}_m(t)$ is defined as a circumference arc whose radius is the mean of sensors radius estimation around it.

$$\begin{aligned} \vec{\Gamma}_m(\alpha) &= (r_m \sin \alpha, r_m \cos \alpha - r_m) \quad 0 \leq |\alpha| \leq \alpha_m \quad \text{such that,} \\ r_m &= \frac{r_n + r_{n+1}}{2} \quad \text{and} \quad d_{st} = \int_{-\alpha_m}^{\alpha_m} \|\vec{\Gamma}_m(\alpha)\| d\alpha = 2|\alpha_m| r_m \end{aligned} \quad (3.23)$$

3.2.2.2 Curvature integration

Curve integration stands for the positioning of both interpolated curves and estimated from strain measurements curves, in accordance with their proper ordination and with the continuity requirement.

Spatial frames and homogeneous transformations are commonly used to define and manipulate mathematical quantities that represent position and orientation of different frames in space. Universal coordinate system is adopted as reference for positions and orientations of each Cartesian coordinate systems (CRAIG, 2005).

These concepts naturally fit to intended curve integration inasmuch as estimated curves are defined with respect to their own reference system. Relative position and orientation are acknowledged by referring each frame $\{F\}_n$ with $n = 1, 2, \dots, N$ and $\{B\}_m$ with $m = 1, 2, \dots, M$ to a universal reference system $\{F\}_0$.

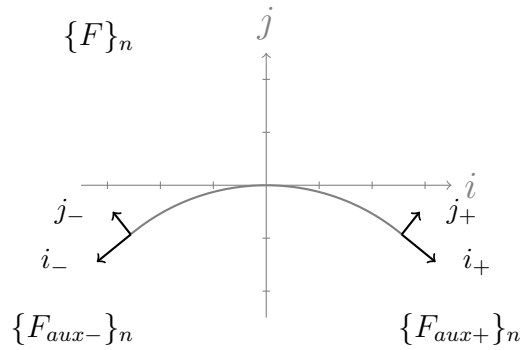


Figure 3.14 – Positive and negative auxiliary frames are attached to the extremities of the estimated curve. i axis has same direction of tangent in that point. It is done similarly to interpolation curves.

For simplicity, it is set that $\{F\}_0 \triangleq \{F\}_1$, being $\{F\}_1$ the reference system of sensor besides reference electrode of EIT belt.

For generic $\vec{\gamma}_n(t)$ and $\vec{\Gamma}_m(t)$, respectively, the n^{th} curvature estimation of sensing segments written on $\{F\}_n$ and the m^{th} interpolation curve connecting n^{th} and $(n+1)^{\text{th}}$ curvature estimations written on $\{B\}_m$, continuity constrain is satisfied when first derivative is continuous along resulting reconstructed curve.

Matching the first derivative of $\vec{\gamma}_n(t)$ positive extremity and the first derivative of $\vec{\Gamma}_m(t)$ negative extremity, it is possible to get, for each interpolation curve m , the constrain equations: $\vec{\gamma}'_n(t_+) - \vec{\Gamma}'_m(t_-) = \vec{0}$ and $\vec{\Gamma}'_m(t_+) - \vec{\gamma}'_{n+1}(t_-) = \vec{0}$.

For further simplifications, a strategy of curves concatenation is done by defining auxiliary frames joint to extremities of both estimated, $\{F_{aux+}\}_n$ and $\{F_{aux-}\}_n$, and interpolated curves, $\{B_{aux+}\}_n$ and $\{B_{aux-}\}_n$. Auxiliary frames have origin on utmost points of the curves, as in figure 3.14. i axis is oriented following first derivative direction at that extremity point and j follows the right-hand rule to be set.

Mathematical mapping operation is, then, used to change descriptions from frame to frame (CRAIG, 2005). In general case, frames might translate with respect to origin points and rotate around axes.

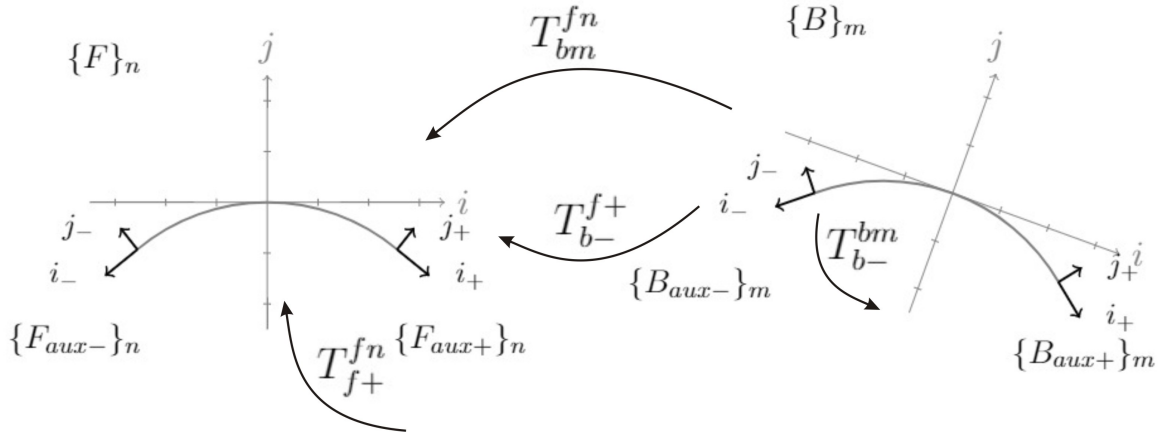


Figure 3.15 – Schematic of homogeneous transformation between the curve estimation n and the interpolating curve m using auxiliary frames to guarantee continuity.

Therefore, homogeneous transformations enable writing each interpolation frame $\{B\}_m$ with respect to curve estimation frame $\{F\}_n$ for $\forall m = n > 0$, and each frame $\{F\}_{n+1}$ in $\{B\}_m$ for $\forall m = n > 0$.

T_{bm}^{fn} is homogeneous transformation operator that permits to write $\{B\}_m$ in $\{F\}_n$, and T_{fn+1}^{bm} that allows $\{F\}_{n+1}$ to be written in $\{B\}_m$. The operators are indirectly derived sequencing transformations based on auxiliary frames constrains, as presented in figure 3.15. Due to property of concatenation of homogeneous transformations:

$$T_{bm}^{fn} = T_{f+}^{fn} T_{b-}^{f+} (T_{b-}^{bm})^{-1} \quad (3.24)$$

$$T_{f+}^{fn} = \begin{bmatrix} \frac{(\vec{\gamma}_n(t_+))' T}{\|\vec{\gamma}_n(t_+)\|} & \frac{(\vec{y}_n(t_+))' T}{\|\vec{y}_n(t_+)\|} & (\vec{\gamma}_n(t_+))' T \\ 0 & 0 & 1 \end{bmatrix} \quad \text{in which} \quad \vec{\gamma}_n(t_+)' \cdot \vec{y}_n(t_+) = 0 \quad (3.25)$$

$$T_{b-}^{bm} = \begin{bmatrix} \frac{(\vec{\Gamma}_m(t_-))' T}{\|\vec{\Gamma}_m(t_-)\|} & \frac{(\vec{Y}_m(t_-))' T}{\|\vec{Y}_m(t_-)\|} & (\vec{\Gamma}_m(t_-))' T \\ 0 & 0 & 1 \end{bmatrix} \quad \text{in which} \quad \vec{\Gamma}_m(t_-)' \cdot \vec{Y}_m(t_-) = 0 \quad (3.26)$$

$$T_{b^-}^{f^+} = \begin{bmatrix} \cos \beta & -\sin \beta & L_x \\ \cos \beta & \sin \beta & L_y \\ 0 & 0 & 1 \end{bmatrix} \quad \text{in which} \quad \beta = \alpha_n - \alpha_m \quad (3.27)$$

L_x and L_y are solved indirectly, applying transformation above in the known extremity points.

The result is equivalently obtained considering the transformation that leads $\{F\}_{n+1}$ to $\{B\}_m$. Once defined the consecutive transformations, pre-multiplication of concatenation property allows to refer all of the curve segments into same absolute reference frame, $\{F\}_0$.

3.3 Curvature simulation

Two curve parametrizations are proposed to shape identification from strain gauge information. For that reason, the behaviors of the approaches for curve reconstruction needs to be mathematically simulated. The investigated methods are: linear approximation with linear interpolation and circumference approximation with mid-radius interpolation.

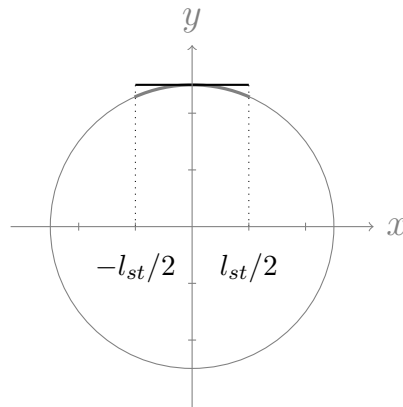


Figure 3.16 – Simulated body shape has circular profile, represented centered in the reference system with axes x and y . Straight element layed on upper-most point of the circumference is a segment of tangent line in that point with dimension equal to strain gauge nominal length.

Simulations are done considering homogeneously circular profiles with different radii and ellipsoidal profiles with different proportions between

semi-major and semi-minor axes. The main intention is understanding limitations of the estimation methods.

To identify deformation from a given curvature, it is defined that strain is related to a given radius.

Thereby, the strain in a given point of the curve is assumed related to the distance of that point and the center of the closed curve. In case of homogeneously circular profiles, the deformation is constant along the whole curve and it is obtained considering the difference between arc length of the simulated curve and tangent line on a given point with strain gauge dimension, l_{st} , as represented in figure 3.16.

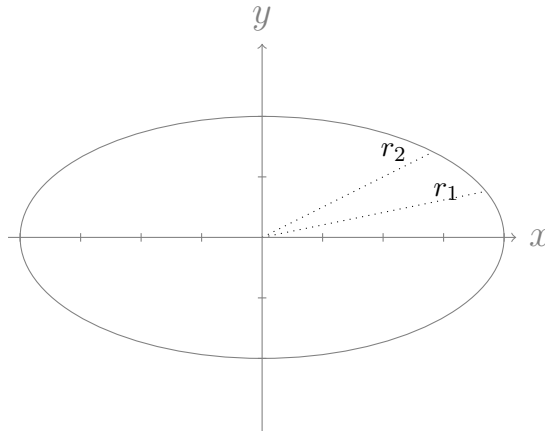


Figure 3.17 – Simulated body shape has ellipsoidal profile, represented centered in the reference system with axes x and y . Strain is considered as the length difference between tangent segment on that point with strain gauge nominal dimension and a circumference arc with radius equal to the distance of the point and ellipse center. Each point of the ellipsoid has equivalent strain approximation of a circumference of radius equal to the distance between ellipse center and the point itself.

Similarly to this hypothesis, in case of ellipsoidal profiles, points belonging to the curve are sampled according to the scale of strain gauge dimension with respect to arc length of ellipse. At each point, strain is considered as the length difference between tangent segment on that point with strain gauge nominal dimension and a circumference arc with radius equal to the distance of the point and ellipse center.

3.3.1 Error propagation

One of the most evident consequence of the type of reconstruction proposed is the error propagation it might lead to. This comes from the fact that each approximation is responsible to a degree of inaccuracy with respect to the segment it intends to estimate. When curve segments are concatenated, the total inaccuracy tends to be a sum of each approximation error.

The error propagation behavior leads to mainly two limitations for the applicability of the system. The restrictions are studied proposing two simulation methods for testing each of reconstruction method developed.

Distance between two strain gauges As mentioned before, an independent variable that may affect estimation accuracy of rounded profiles is the length of non-monitored segments of the belt, that is, the distance between two strain gauges, d_{st} . The establishment of this value is relevant to the reduction of the number of sensors, thereby allowing the applicability of the device in real clinical cases.

Simulations are done setting a fixed body radius and considering a belt with length equal to body shape contour dimension. Results are obtained plotting reconstructed line with respect to expected body shape varying variable d_{st} . d_{st} is defined proportional to strain gauge length, l_{st} .

Body radius variation To be applicable in human thorax shape identification, the methods have to be able to detect circumferences that ranges around the standard values of human thorax dimensions.

The study intends to simulated behavior of reconstruction method when exposed to body shapes with radii varying from 200 mm to 50 mm. Hence, it is imposed a constant distance between strain gauges and a belt length equal to body shape contour dimension.

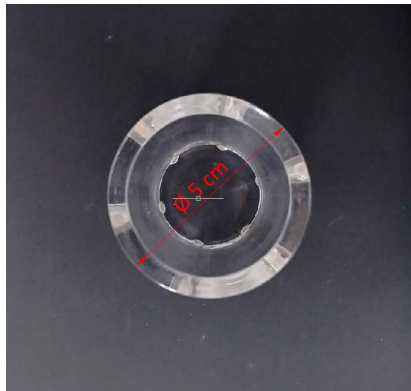
Elliptical body shape This test aims to understand behavior of both methods when exposed to curvature variation within same set of information. Thereby, simulations with elliptical curves with different

proportions of semi-major and semi-minor axes are done for both methods.

3.4 System evaluation methods

Experimentation of the shape identification system is branched into validation of curve reconstruction method and sensing circuit, aside and jointly.

After simulating reconstruction methods, empirical test is proposed to evaluate circuitry functioning and reconstruction quality. Due to reconstruction method characteristics, it is necessary to valid reconstruction results at least three sensing elements along the experimental belt.



(a) Probe with $D = 50$ mm



(b) Probe with $D = 50$ mm in test configuration



(c) Probe with $D = 200$ mm



(d) Probe with $D = 200$ mm in test configuration

Figure 3.18 – Specimens used in experimentation to simulate range of human body thorax dimensions.

The test procedure consists on (a) calibrating measurement system with respect to the flat reference surface and (b) attaching the sensing belt

to the specimen. After transitory response of the measurement system, data from Arduino is acquired. Each selected specimen is submitted to the test three times.

Due to expected thorax dimensions, selected samples are two bodies with circle profile with diameter of 50 mm and 200 mm, as shown in figure 3.18.

Source of uncertainties during a measurement are multiple, either from physical structure as fixation imperfections of strain gauges on backing, circuit components tolerance values and power source fluctuations, as from reconstruction method approximations such as numerical truncation and modeling mismatching.

Therefore, it ought to qualify errors in reconstruction method results under EIT scenario. The error analysis is done in two steps, described in next subsections.

3.4.1 Precision

Precision describes measure variation when done repeatedly under the same conditions experiments (HOLMAN; GAJDA, 2001). Therefore, to estimate precision of measurements it is firstly necessary to consider the average curve, \bar{X} , of three tests for each specimen. However, by processing the curve in MATLAB software, the final curve is actually discretized in a finite number of points, I , as defined by the program.

$$\bar{X} = \{\bar{x}_0, \bar{x}_1, \dots, \bar{x}_I\} \quad \text{where} \quad \bar{x}_i = \frac{x_{i1} + x_{i2} + x_{i3}}{3} \quad (3.28)$$

Variance is then obtained for each point i , as:

$$\sigma_i^2 = \sum_{j=1}^3 \frac{(x_{ij} - \bar{x}_i)^2}{3 - 1} \quad (3.29)$$

Average variance and mean variance are good indicators of precision

of experimental results in this case:

$$\bar{\sigma}^2 = \sum_{i=1}^I \frac{\sigma_i^2}{I} \quad \text{and} \quad \sigma_{max}^2 = \max_i \sigma_i^2 \quad (3.30)$$

3.4.2 Accuracy

The accuracy of an instrument indicates the deviation of the reading from a known input (HOLMAN; GAJDA, 2001). Since specimens have constant radius, comparison between real value and measurement obtained can be quantified with maximum absolute deviation error, δx_{max} , of radius of each point of average curve, \bar{r}_i , with respect to specimen one r .

$$\delta x_{max} = \max_i |\bar{r}_i - r| \quad (3.31)$$

Maximal percentile deviation error, η_{max} , and average percentile deviation error, $\bar{\eta}$, are also considered in accuracy analysis:

$$\eta_{max} = \frac{\delta x_{max}}{r} 100 \quad (3.32)$$

$$\bar{\eta} = \frac{\sum_{i=1}^I \delta x_i}{I r} 100 \quad (3.33)$$

4 RESULTS

4.1 Shape identification device

4.1.1 Belt configuration

Following requirements presented before, sensing belt segment was built on polypropylene backing with 0.18 mm thick, which entails enough flexibility and low elasticity. According to chapter 3 and figure 3.6, sensors are fixed symmetrically in both sides of backing material.

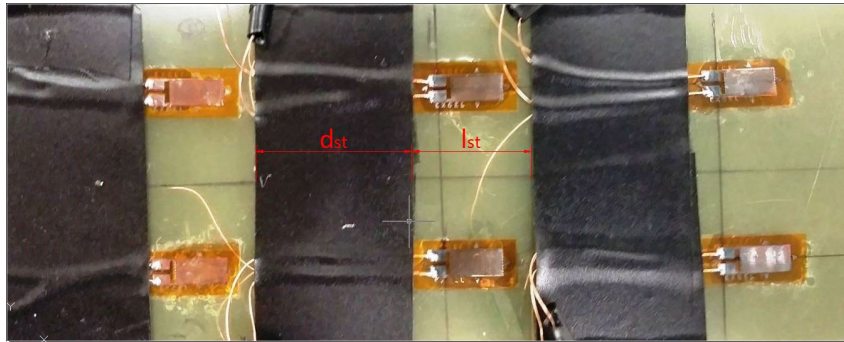


Figure 4.1 – Yellow backing material over which strain gauges are fixed with glue and their cables set stable with black insulating tape. The total test belt is composed by 3 sensing segments and two sensing gaps equally distributed.

The strain gauge model used in this project is the PA-060259BA-120, presented in chapter 3 which is a general-purpose foil strain gauges for low-elasticity materials with vinyl-coated flat cable. The sensor is manufactured on a thin plastic layer which is fixed with cyanoacrylate glue.

Three sets of sensors were considered along the belt, each set instead was assembled with four sensors. In total, the testing belt was made by twelve sensors costing around 75 dollars.

The disposal of strain gauges along belt, defined by d_{st} , was simulated before attaching sensors to backing material, as discussed in subsection 4.2. At the final configuration, figure 4.1, non-sensing segment length, d_{st} , was defined as 25.4 mm, which means 4 times the sensor's length, l_{st} .

The errors with respect to mismatching of real and estimated reference center line are reduced by the low thickness of backing material. However, fixation procedure may also lead to behavior errors of bonding condition, since glue adds a degree of rigidity to sensors when dried.

Moreover, to avoid interference and short-circuit, measurements were made with a shield material around the belt, with same isolate material of the belt structure.

Although achieving a satisfactory resultant belt, the available strain gauges had a great degree of brittle. Due to their difficult handling, losses of 25% of the acquired sensors were provoked when manufacturing the belt.

Moreover, it was verified self-heating phenomenon even if sensors were powered to specified current. According to [Hoffmann \(1989\)](#), pulse supplies would be a suitable method of overcoming problems due to high self-heating with strain gages.

4.1.2 Electronic circuit

Circuitry, described in section 3.1.3, was reproduced three times in this project to provide signal conditioning for the three sensing segments of figure 4.1. It was built over a test board to which the signal input arrives from sensors. The board contains the Wheatstone bridges balanced by the trimming potentiometers, INA amplifiers with equally established gain and output connection with Arduino board.

Considering voltage and current requirements, circuit, represented in figure 3.9, has its independent variables designed as in table 4.1.

Calibration pins were placed at the output pins of INA components to facilitate adjustments through external voltage measuring devices.

A laboratory multi-voltage font was used to supply different voltages and currents demanded for the conditioning circuit elements, since amplifiers and summing circuits require symmetrical source of ± 15 V, while strain gauge bridge and Arduino board are powered by 5 V. Thereby, power supply was set at ± 15 V and 5 V with same ground reference and with constant current amplitude about 5 mA. For real applications, however, circuits to

Table 4.1 – Elements selection according to circuitry project.

Component	Value	Unit
Resistance (R_B)	15	k Ω
Resistance (R_E)	1.2	k Ω
Diode 1N1104 (V_{dd})	0.7	V
Transistor PNP 2N2907 (V_t)	0.7	V
Offset trimpot (R_c)	0 – 10	k Ω
Amplifier gain (R_G)	1	k Ω
Bridge trimpot (R_t)	0 – 10	Ω

land symmetric voltages from constant positive power suppliers might be considered.

Additionally, the crossing of cables around the test board causes certain signal instability due to the order of magnitude signals from sensor have. For that reason, it is preferred to manufacture the sensor conditioning circuit in printed circuit boards and to further design sensing belt and cables disposals.

4.1.3 Calibration results

A rigid insulating surface was set as flat calibration reference. For each calibration step required for the tests of this project, the belt was attached to the reference surface with insulating tape to guarantee immobility and flat adherence.

With the help of a multimeter, after the testing belt is fixed on the reference surface, the calibration pins were set to zero, balancing Wheatstone bridges by the variation of trimming potentiometers. Once balanced, the probe was place in the output pins of the conditioning circuit, that are connected to the Arduino board. By changing the summing circuit trimming potentiometer, the offset in null strain gauge deformation was set at 2.5 V, according to the definitions of chapter 3.

Calibration procedure needed to be reviewed after each test mainly due to the instability the board imposed to the system. Moreover, a hysteresis phenomenon was noted in sensor's behavior after being attached to

a surface test and then to the reference flat surface.

The mechanical hysteresis of a strain gage is the difference in the measured value for rising and falling strain loadings with the same strain value on the specimen. The literature determines that the largest difference in the zero point on the abscissa of a curve for tension rising and falling through a complete cycle may achieve values from $\pm 1000 \mu\text{m m}^{-1}$ to $\pm 3000 \mu\text{m m}^{-1}$ (HOFFMANN, 1989).

The selection of different strain gage grid designs and adhesives may be sufficient to significantly reduce in hysteresis according to Hoffmann (1989), as in figure 4.2.

4.2 Curvature simulation

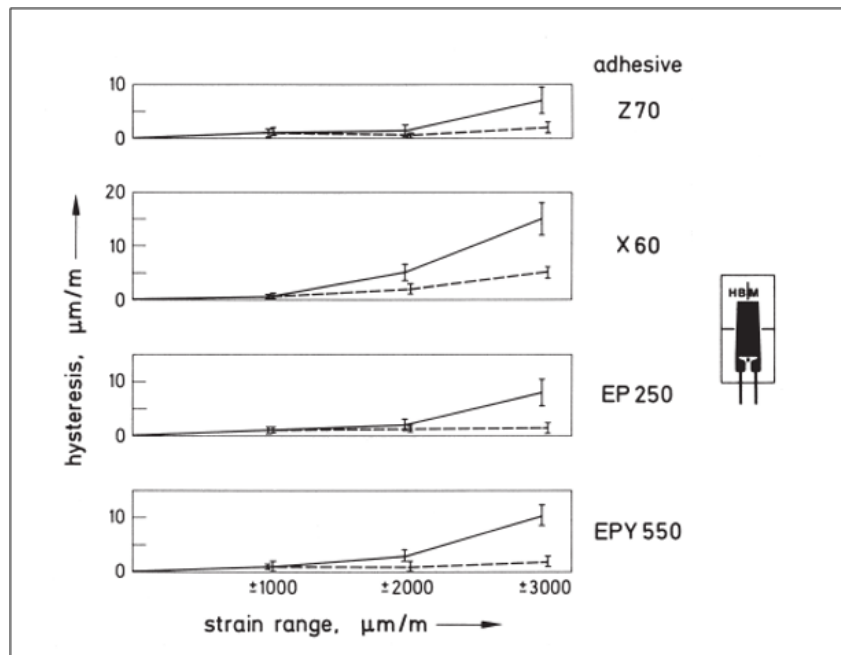
Simulations were done to analyze mainly two important aspects of estimation, which are the disposal of sensing elements along the belt and the dimension limitations of the methods. According to the methodology proposed in section 3.3, the following tests were done.

4.2.1 Distance between two strain gauges

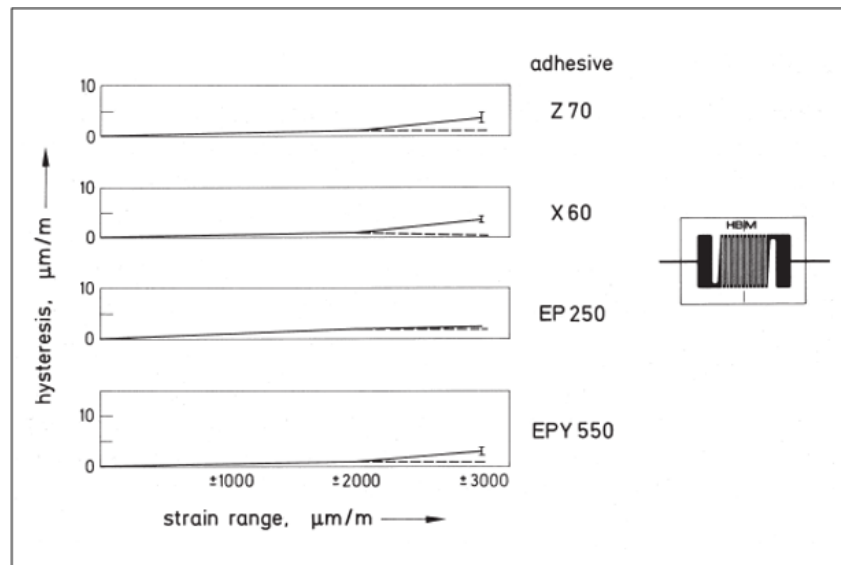
Ideally, the belt should have its length completely monitored with strain gauges in order to decrease inferences that may cause inaccuracy. Although it is possible to decrease d_{st} (figure 3.2b and figure 4.1), it is physically and economically unfeasible.

For this reason, researches were made to simulate the impacts on reconstruction methods from distances proportions of d_{st} and l_{st} . In all simulations, testing circumference is constant in 100 mm, l_{st} is assumed 6 mm while d_{st} varies proportionally to it, as shown in figures 4.3a and 4.3b.

It is possible to perceive linear approximation with relevant d_{st} does not present good results with large belt length considered. Additionally, greater is the non sensitive length approximation rapidly deviate from expected result.

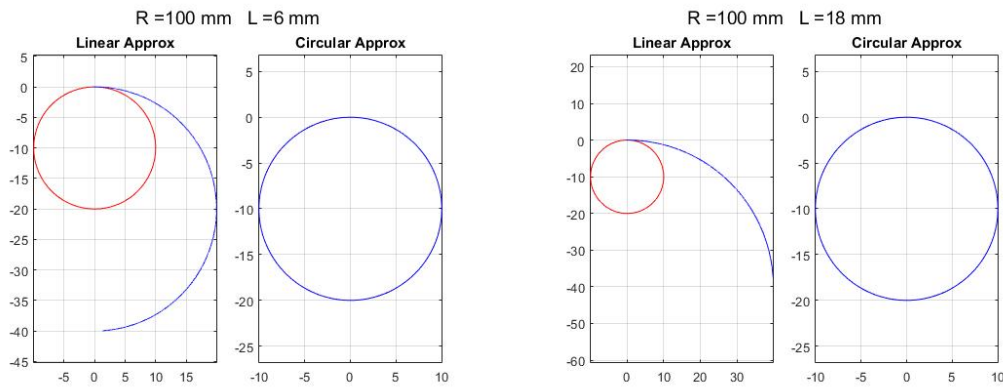


(a) Mechanical hysteresis for the strain gage type LY 11 6/120, bonded with 4 different adhesives.



(b) Mechanical hysteresis of the strain gage type LY 21 6/120, bonded with four different adhesives.

Figure 4.2 – (a) and (b) are taken from (HOFFMANN, 1989). Dashed line represents the third cycle of rising and falling strain loads while the whole line is resultant of the first cycle. Z 70 is a cold curing rapid adhesive based on cyano acrylate, X 60 is also a cold curing rapid adhesive but based on polymethacrylate and the two adhesives EP 250 and EPY 550 are hot curing epoxy resin adhesives



- (a) Non-sensing segment is set equal to sensors length. On the left, the linear approximation result presents a great variation between real testing line (red) and estimated line (blue). On the right, with circular approximation technique, the difference between real testing line and estimated one are not noticeable .
- (b) Non-sensing segment is set as the double of sensors length. On the left, linear approximation result presents a great variation between real testing line (red) and estimated line (blue). On the right, with circular approximation technique, the difference between real testing line and estimated one are not noticeable.

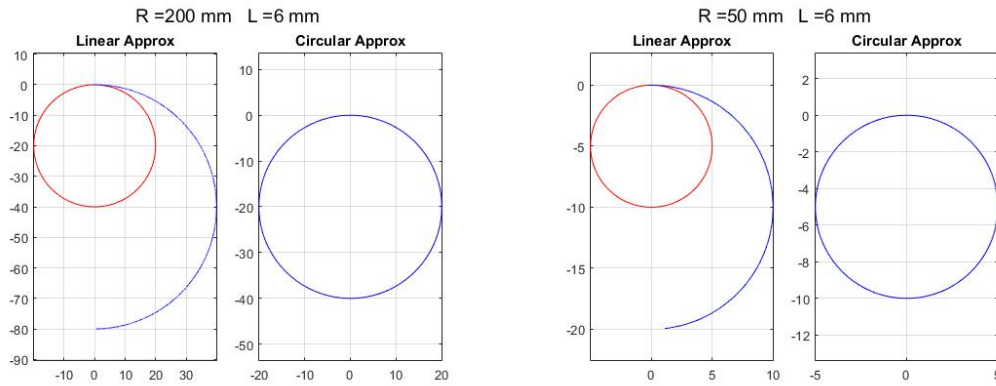
Figure 4.3 – Simulation results for distance between two strain gauges. The distances selected are proportional to the nominal length of strain gage sensor and the body radius is constant 100 mm. (a) refers to a distance equal to the nominal length. (b) is the result for a distances between two strain gages equal to three times the nominal length of the sensors.

In the case of circular approximation technique, no relevant deviation was identified, appearing to be the most consistent method of both. It was defined that in experimental system d_{st} is 4 times l_{st} , as it was understood to facilitate physical construction without disturb, results in circular approximation.

4.2.2 Body radius variation

This simulation intends to visualize if methods are able to correctly estimate the curvature inside human body ranges.

Therefore, another two testing curves were defined as circles with radius of 200 mm and 50 mm which are comparable with anterior and lateral curvatures of human thorax.



- (a) Testing maximum radius variation with constant d_{st} value. On left side, linear approximation presents significant differences between expected curve (red) and the estimated one (blue). On the right side, the difference between real testing line and the estimated one is not noticeable.
- (b) Testing minimum radius variation with constant d_{st} value. On left side, linear approximation presents significant differences between expected curve (red) and estimated one (blue). On right side, the difference between real testing line and the estimated one is not noticeable.

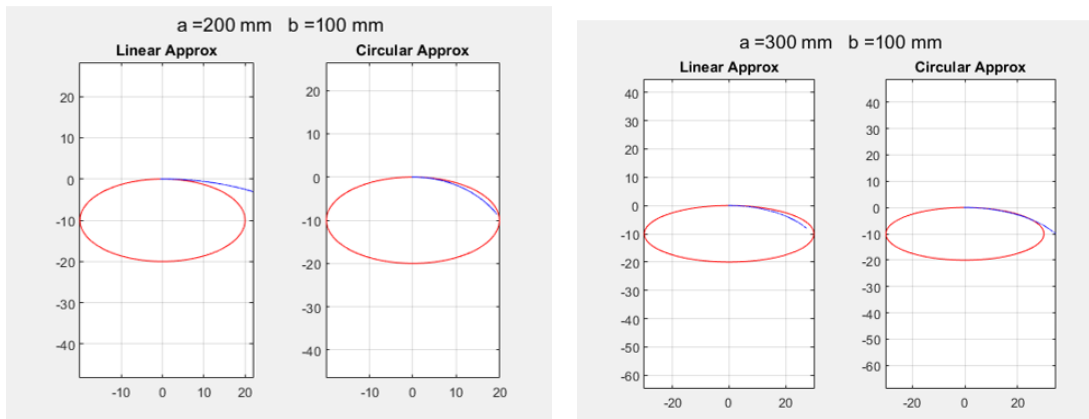
Figure 4.4 – Simulation results body radius variation within the range of human thorax dimensions. (a) is the simulation for a circular body shape with radius of 200 mm. (b) is the result for a circular body shape with radius of 50 mm

Furthermore, to reduce superimposition of effects, d_{st} was selected as equal to sensors length. Simulation results, in figure 4.4b, confirms circular approximation method based on medium curvature estimation may be the most affordable one for required ranges of sensing belt applications.

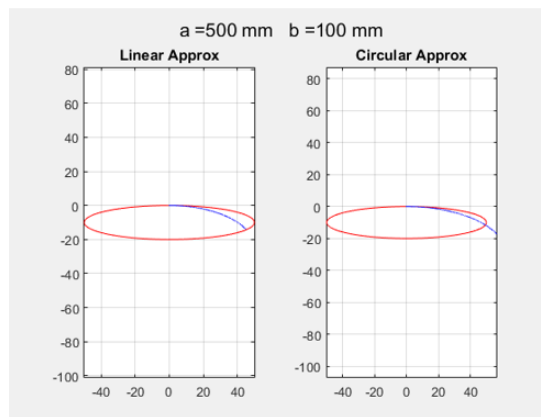
4.2.3 Elliptical body shape

The simulation intends to understand the behavior of both methods when curvature along the contour is not constant. For simplicity it was select an elliptical profile due to the possibility of curve parametrization.

Under the hypothesis of simulation defined in section 3.3, it was defined a constant ratio of the length between strain gauges and the nominal dimension of strain gauge equals to one. Additionally, the total simulated length was correspondent for the first quadrant of the ellipse curve. Three tests were done with varying the proportion between semi-major and semi-minor axes of elliptical profiles.



(a) a is set equal to 200 mm. b is set equal to 100 mm. (b) a is set equal to 300 mm. b is set equal to 100 mm.



(c) a is set equal to 500 mm. b is set equal to 100 mm.

Figure 4.5 – Testing proportion between semi-major, a and semi-minor axes, b , of elliptical profile. Simulation results body format variation within the ranges of human thorax. On left side, linear approximation is represented (blue). On right side, mid-curve estimation is represented (blue). Red line is the expected curve.

From figure 4.5, it is possible to notice that both methods present relevance when curvature is not constant. While the circular approximation with mid-curve estimation performs better with almost circular profiles, figure 4.5a, linear approximation with linear interpolation is capable to estimate segments of flatter shapes, figures 4.5b and 4.5c.

4.3 System evaluation

The experimentation method uses the circuit developed before integrated to the mathematical method developed in MATLAB.

For the experiment, a connection of conditioning circuit with Arduino Mega2560 board was made, and with the help of MATLAB library for hardware input information, signals from analog input pins of the board were read. The Analog-to-Digital conversion of the signal was done considering the resolution of the board (described in section 3.1.3).

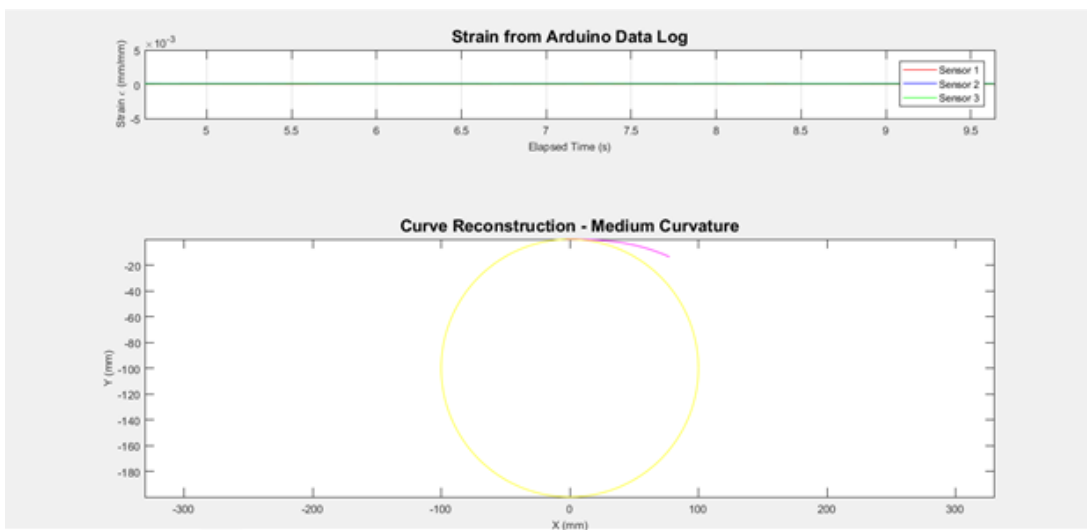


Figure 4.6 – Experience with belt in neutral flat position. Data Log of Arduino board is the upper-most plot, in which is possible to notice that three sensors have strain in zero position. Second graph is resultant of reconstruction method applied in neutral position: magenta line is the reconstructed final curve.

The strain information was, then, treated by the reconstruction method which estimates sensors curvature using circumference approximation and interpolation curves with mid-radius interpolating curve. This method was select due to simulations presented before whose results demonstrated that for homogeneous circular profiles circumference approximation with mid-radius interpolation is consistent for any distance between two strain gauges and for any specimen radius.

From table 4.1, the nominal resistance of trimming potentiometers, R_t , used for balancing Wheatstone bridge is less then 8.4% of the nominal

resistance of strain gage sensor. For that reason, equation 3.11 is valid and is the final transfer function for the experiment. The gain of INA amplification step was set equal to 59.4 and the offset 2.5 V.

Following the experimental procedure described in chapter 3, the first practice of each test is the calibration over a flat surface. In figure 4.6, there are represented results of reconstructed model when belt is at neutral position after calibration.

Although it is not feasible to quantify the flatness of calibration surface to compare to the result obtain, by visualizing the plot it is possible to acknowledge that the reconstruction line is representative of physical situation of the sensing belt. Calibration is also verified in the upper-most subplot of figure 4.6 in which input signals of the three sensing segments present equivalent zero strain.

Three tests were performed for both specimen. However, output signal from microcontroller board was noisy disrupted. For this reason, for each test performed, samples were taken along 30 s after stationary condition was stabilized with a time step of 5 seconds between each of them. The mean curve of the six curves acquired was considered the final curve of the test.

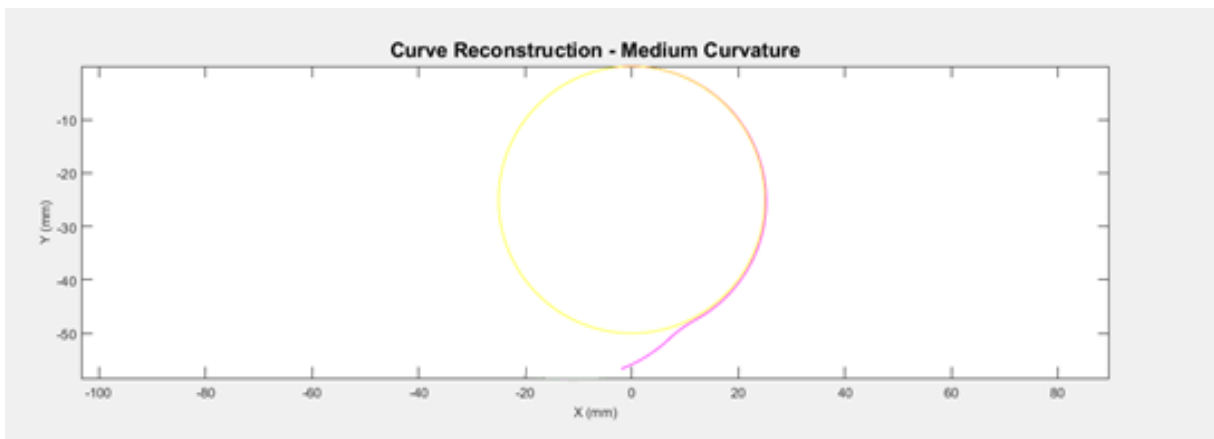


Figure 4.7 – Mean curve for specimen of $D = 50mm$ obtained after reconstruction method is represented by magenta line, while the yellow one is the expected curve of the body.

After repeating the test procedure three times, it was calculated total mean curve as well as errors index described in last chapter. Figures 4.7

and 4.8 represents the mean curves obtained after tests in specimen with 50 mm and 200 mm of diameter, respectively.

From figure 4.7, the estimation curve provided by the reconstruction method of circumference approximation and mid-radius interpolation is able to describe consistently most part of the circumference arc over which the testing belt is affixed. However, the last portion of the line presents a greater deviation from the expected curve with respect to the rest of the reconstructed line.

Table 4.2 – Error index values for tests in specimen with $D = 50mm$

Error Index	Value	Unit
$\bar{\sigma}^2$	520.80	mm ²
σ_{max}^2	1821.42	mm ²
δx_{max}	6.79	mm
η_{max}	27.16	%
$\bar{\eta}$	10.86	%

Two aspects were hypothesized to explain this behaviour: the error propagation of sequential concatenation of curves but also the mechanical interference the remaining part of the belt may cause due to the difficult to attach the whole belt around the specimen.

Even though, considering the experiment with specimen of $D = 50mm$ as the most critical due to the degree of bending sensor is exposed to, the resultant error indexes, table 4.2, are consistent to empirical electronic results.

The reconstructed curve of second circular body, $D = 50mm$, was obtained following same conditions of the first one. The resultant curve, represented in figure 4.8, had low deviation from the expected curve. However, same effect of increasing deviation at the end of estimated line is present but with lower amplitude with respect to the first test.

From table 4.3, the error indexes are presented for the second specimen after performing three test procedures. It is easy to see the errors significantly decreased considering different body shapes.

Although not directly tantamount to results of this project, the

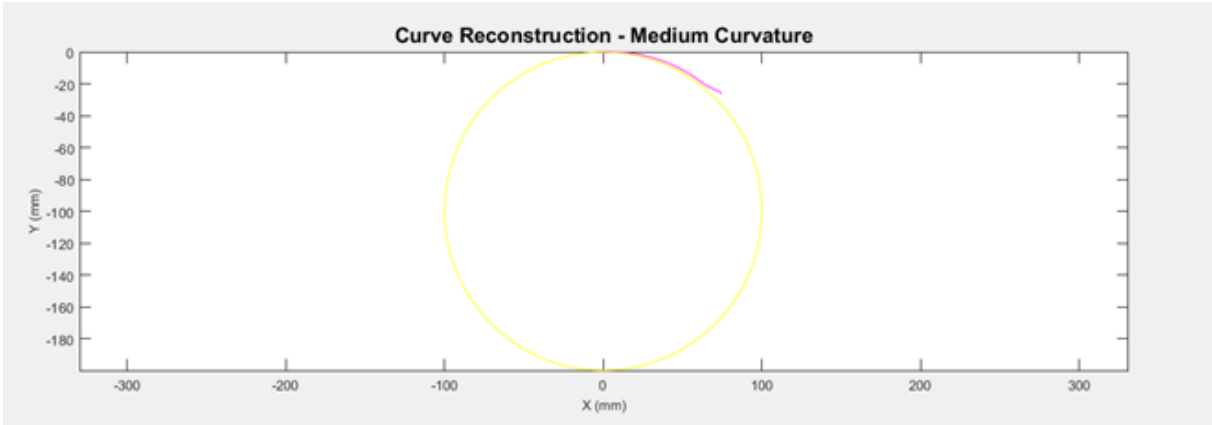


Figure 4.8 – Mean curve for specimen of $D = 200\text{mm}$ obtained after reconstruction method is represented by magenta line, while the yellow one is the expected curve of the body.

Table 4.3 – Error index values for tests in specimen with $D = 200\text{mm}$

Error Index	Value	Unit
$\bar{\sigma}^2$	1001.6	mm^2
σ_{max}^2	2914.32	mm^2
δx_{max}	13.3	mm
η_{max}	13.35	%
$\bar{\eta}$	5.05	%

conclusions of this work are better understood when compared to imaging errors of EIT technology context present in literature. It is not an easy task to define errors of this particular imaging technique since it is based on a nonlinear inverse boundary value problem which is highly unstable with respect to measurement and modeling errors.

According to the study of [Nissinen et al. \(2011\)](#) which proposes an adaptation of approximation error approach to compensate for the modeling errors caused by inaccurately known body shape, simulations of thorax imaging with compensation of errors approach reveal a relative estimation error that ranges between 36.62% to 11.01%.

Despite that, many improvements are still considered to electronic approach for body shape estimation using strain gauge sensors. As mentioned along the chapter, actions to improve signal and calibration stability and to refine reconstruction method to increase accuracy and reduce error propagation would enhance performance of the system.

5 DISCUSSION AND CONCLUSION

In this thesis, an electronic system able to identify electrode positioning and body shape curvature in an EIT was projected and realized. Among existing technologies, strain gauge was selected due to its biocompatibility, low invasibility and small size.

The prototype was made of a polypropylene backing belt that guarantees flexibility but with low elasticity. Every sensor was conditioned by a Wheatstone bridge which connects four identical strain gauges disposed in both sides of strap, as shown in figure 3.6, to obtain linearity and enhance accuracy when measuring bending deformation.

From proposed mathematical models, circumference approximation with mid-radius interpolation seemed to provide the most consistent results for shapes with almost circular contour. However, linear approximation with linear interpolation demonstrated a good performance for flatter body shapes. Strain gauges are able to sense contour of only a small segment. A future development would be the composition of both methods according to real curvature measurements.

Applying this electronic system to a real object, the reconstructed curve presents low deviations from the real one. This might mean approximation method and strain gauges sensing circuit could have a promising application in the EIT field with further developments. More studies about disposal of strain gauges along the belt will be able to improve approximation considering thoracic dimensions.

To reduce the discrepancy in the results, an improvement of the sensing device is suggested, overcoming hysteresis phenomena and unstable conditions. Moreover, the inclusion of a filter may attenuate noise which, at the moment, has a relevant impact in the low magnitude order of signal voltage. Adding a filtering phase would also be interesting to signal perception especially in boundary conditions, such as when measuring circumferences has radius tending to infinite, flat surface.

From the economical point of view, the use of such widespread technology as strain gauges allow economic feasibility, even if it was not the first scope of the project. For a condition in which the whole belt is sensed by strain gauges, following the belt configurations discussed before, it is estimated a cost of 750 dollars for the equipment. An implementation of the circuit in a printed circuit board, PCB, should be done for reducing signal interference, increasing accuracy.

This thesis proposes to be a starting point of shape reconstruction technique using electronics particularly based on strain gage technology. Yet, its results already might benefit other advanced methods of curvature estimation in EIT context, such as the simultaneous reconstruction method (DARDÉ *et al.*, 2013b) and compensation of modelling errors (NISSINEN *et al.*, 2011) whose performance are enhanced with the knowledge of any boundary shape information.

Further development for this thesis can be the shape reconstruction of 3-dimensional shapes and the use of more generic parametric equations when estimating curves. However, the circumference approximation should remain relevant to a 2-D estimation of human thorax contour, composed by a sequence of curves.

The final aim of the usage of strain gauges in the EIT is the application to a real case. With this thesis and further mentioned developments, advancements in imaging quality of this promising biomedical imaging technology are expected, increasing the clinical relevance of EIT imaging has.

BIBLIOGRAPHY

ADLER, A.; AMYOT, R.; GUARDO, R.; BATES, J.; BERTHIAUME, Y. Monitoring changes in lung air and liquid volumes with electrical impedance tomography. *Journal of Applied Physiology*, Am Physiological Soc, v. 83, n. 5, p. 1762–1767, 1997.

AGUIAR, E. D.; STOLL, C.; THEOBALT, C.; AHMED, N.; SEIDEL, H.-P.; THRUN, S. Performance capture from sparse multi-view video. In: ACM. *ACM Transactions on Graphics (TOG)*. [S.l.], 2008. v. 27, n. 3, p. 98.

ARDUINO. *Arduino Mega ADK*. 2018. Accessed: 2018-02-07. Disponível em: <https://www.arduino.cc/en/Main/ArduinoBoardMegaADK?from=Main.ArduinoBoardADK>.

BARBER, D. C.; BROWN, B. H. Applied potential tomography. *Journal of Physics E: Scientific Instruments*, IOP Publishing, v. 17, n. 9, p. 723, 1984.

BROWN, R. *Kinect Intermedial Performance and Improvisation*. 2017. Accessed: 2017-10-05. Disponível em: <http://kinectic.net/motion-capture-face/>.

BURR-BROWN CORPORATION. *Precision, Low Power Instrumentation Amplifiers*. [S.l.], 1996.

CHENEY, M.; ISAACSON, D.; NEWELL, J. C. Electrical impedance tomography. *SIAM review*, SIAM, v. 41, n. 1, p. 85–101, 1999.

CHENG, K.-S.; ISAACSON, D.; NEWELL, J.; GISSER, D. G. Electrode models for electric current computed tomography. *IEEE Transactions on Biomedical Engineering*, IEEE, v. 36, n. 9, p. 918–924, 1989.

COSTA, E. L.; LIMA, R. G.; AMATO, M. B. Electrical impedance tomography. *Intensive Care Medicine*, Springer, p. 394–404, 2009.

CRAIG, J. J. *Introduction to robotics: mechanics and control*. [S.l.]: Pearson Prentice Hall Upper Saddle River, 2005. v. 3.

DARDÉ, J.; HYVÖNEN, N.; SEPPÄNEN, A.; STABOULIS, S. Simultaneous recovery of admittivity and body shape in electrical

- impedance tomography: an experimental evaluation. *Inverse Problems*, IOP Publishing, v. 29, n. 8, p. 085004, 2013.
- DARDÉ, J.; HYVONEN, N.; SEPPANEN, A.; STABOULIS, S. Simultaneous reconstruction of outer boundary shape and admittivity distribution in electrical impedance tomography. *SIAM Journal on Imaging Sciences*, SIAM, v. 6, n. 1, p. 176–198, 2013.
- DELP, S. L.; ANDERSON, F. C.; ARNOLD, A. S.; LOAN, P.; HABIB, A.; JOHN, C. T.; GUENDELMAN, E.; THELEN, D. G. Opensim: open-source software to create and analyze dynamic simulations of movement. *IEEE transactions on biomedical engineering*, IEEE, v. 54, n. 11, p. 1940–1950, 2007.
- FITZGIBBON, A. W.; ZISSERMAN, A. Automatic camera recovery for closed or open image sequences. In: SPRINGER. *European conference on computer vision*. [S.l.], 1998. p. 311–326.
- GABRIEL, S.; LAU, R.; GABRIEL, C. The dielectric properties of biological tissues: Iii. parametric models for the dielectric spectrum of tissues. *Physics in medicine and biology*, IOP Publishing, v. 41, n. 11, p. 2271, 1996.
- GÓMEZ-LABERGE, C.; ADLER, A. Direct eit jacobian calculations for conductivity change and electrode movement. *Physiological measurement*, IOP Publishing, v. 29, n. 6, p. S89, 2008.
- HENRY, P.; KRAININ, M.; HERBST, E.; REN, X.; FOX, D. Rgb-d mapping: Using kinect-style depth cameras for dense 3d modeling of indoor environments. *The International Journal of Robotics Research*, SAGE Publications Sage UK: London, England, v. 31, n. 5, p. 647–663, 2012.
- HOFFMANN, K. *An introduction to measurements using strain gages*. [S.l.]: Hottinger Baldwin Messtechnik Darmstadt, 1989.
- HOLDER, D. S. *Electrical impedance tomography: methods, history and applications*. [S.l.]: CRC Press, 2004.
- HOLMAN, J. P.; GAJDA, W. J. *Experimental methods for engineers*. [S.l.]: McGraw-Hill New York, 2001. v. 2.
- JEHL, M.; AVERY, J.; MALONE, E.; HOLDER, D.; BETCKE, T. Correcting electrode modelling errors in eit on realistic 3d head models. *Physiological measurement*, IOP Publishing, v. 36, n. 12, p. 2423, 2015.

LAWSON, C. M.; TEKIPPE, V. Fiber-optic diaphragm-curvature pressure transducer. *Optics letters*, Optical Society of America, v. 8, n. 5, p. 286–288, 1983.

LIONHEART, W. R. Boundary shape and electrical impedance tomography. *Inverse Problems*, IOP Publishing, v. 14, n. 1, p. 139, 1998.

NATIONAL INSTRUMENTS. *Strain Gauge Measurement – A Tutorial*. [S.l.], 1998. Application Note 078.

NEWCOMBE, R. A.; IZADI, S.; HILLIGES, O.; MOLYNEAUX, D.; KIM, D.; DAVISON, A. J.; KOHI, P.; SHOTTON, J.; HODGES, S.; FITZGIBBON, A. Kinectfusion: Real-time dense surface mapping and tracking. In: IEEE. *Mixed and augmented reality (ISMAR), 2011 10th IEEE international symposium on*. [S.l.], 2011. p. 127–136.

NISSINEN, A.; KOLEHMAINEN, V. P.; KAIPIO, J. P. Compensation of modelling errors due to unknown domain boundary in electrical impedance tomography. *IEEE Transactions on Medical Imaging*, IEEE, v. 30, n. 2, p. 231–242, 2011.

NOIUMKAR, S.; TIRAKOAT, S. Use of optical motion capture in sports science: A case study of golf swing. In: IEEE. *Informatics and Creative Multimedia (ICICM), 2013 International Conference on*. [S.l.], 2013. p. 310–313.

Northern Digital Inc. *NDI Medical Optical Measurement Systems*. 2017. Accessed: 2017-10-05. Disponível em: <https://www.ndigital.com/medical/products/>.

NORTON, K.; OLDS, T. *Anthropometrica: a textbook of body measurement for sports and health courses*. [S.l.]: UNSW press, 1996.

OLIVEIRA, T. F. de. *Transdutores de Ultrassom Multielementos Lineares Flexíveis com Sensor de Curvatura para Superfícies Curvas*. Tese (Doutorado) — Universidade de São Paulo, 2015.

SEITZ, S. M.; CURLESS, B.; DIEBEL, J.; SCHARSTEIN, D.; SZELISKI, R. A comparison and evaluation of multi-view stereo reconstruction algorithms. In: IEEE. *Computer vision and pattern recognition, 2006 IEEE Computer Society Conference on*. [S.l.], 2006. v. 1, p. 519–528.

SILVA, A.; CARMO, J.; MENDES, P.; CORREIA, J. Simultaneous cardiac and respiratory frequency measurement based on a single fiber bragg

- grating sensor. *Measurement Science and Technology*, IOP Publishing, v. 22, n. 7, p. 075801, 2011.
- SOLEIMANI, M.; GÓMEZ-LABERGE, C.; ADLER, A. Imaging of conductivity changes and electrode movement in eit. *Physiological measurement*, IOP Publishing, v. 27, n. 5, p. S103, 2006.
- SZELISKI, R. *Computer vision: algorithms and applications*. [S.l.]: Springer Science & Business Media, 2010.
- TAFFONI, F.; FORMICA, D.; SACCOMANDI, P.; PINO, G. D.; SCHENA, E. Optical fiber-based mr-compatible sensors for medical applications: An overview. *Sensors*, Multidisciplinary Digital Publishing Institute, v. 13, n. 10, p. 14105–14120, 2013.
- TESCHNER, E.; IMHOFF, M.; LEONHARDT, S. *Electrical Impedance Tomography: The realisation of regional ventilation monitoring*. 2. ed. [S.l.]: Drägerwerk AG Co. KGaA, 2010.
- TEXAS INSTRUMENT. *INA12x Precision, Low-Power Instrumentation Amplifiers*. [S.l.], 1995. Revised January 2018.
- TONG, J.; ZHOU, J.; LIU, L.; PAN, Z.; YAN, H. Scanning 3d full human bodies using kinects. *IEEE transactions on visualization and computer graphics*, IEEE, v. 18, n. 4, p. 643–650, 2012.
- WEBSTER, J. G. Medical instrumentation-application and design. *Journal of Clinical Engineering*, LWW, v. 3, n. 3, p. 306, 1978.
- YI, X.; NIU, F.; HE, J.; FAN, H. The 3d shape analysis of elastic rod in shape sensing medical robot system. In: IEEE. *Robotics and Biomimetics (ROBIO), 2010 IEEE International Conference on*. [S.l.], 2010. p. 1014–1018.
- YORKEY, T.; WEBSTER, J. A comparison of impedance tomographic reconstruction algorithms. *Clinical Physics and Physiological Measurement*, IOP Publishing, v. 8, n. 4A, p. 55, 1987.